Eur. Phys. J. C (2026) 86:643
https://doi.org/10.1140/epjc/s10052-026-15817-7

THE EUROPEAN PHYSICAL JOURNAL C

Regular Article - Theoretical Physics

Higgs boson decays $h \to Z\gamma$ and $h \to m_V Z$ in the $U(1)_X$VLFM

Rong-Zhi Sun[1,2,3], **Shu-Min Zhao**[1,2,3,a], **Yue-Tong Liu**[1,2,3], **Xing-Xing Dong**[1,2,3,4,b]

[1] Department of Physics, Hebei University, Baoding 071002, China
[2] Hebei Key Laboratory of High-precision Computation and Application of Quantum Field Theory, Baoding 071002, China
[3] Hebei Research Center of the Basic Discipline for Computational Physics, Baoding 071002, China
[4] Departamento de Fisica and CFTP, Instituto Superior Técnico, Universidade de Lisboa, Av. Rovisco Pais 1, 1049-001 Lisbon, Portugal

Received: 19 January 2026 / Accepted: 8 May 2026

Abstract We study the Higgs boson decays $h \to Z\gamma$ and $h \to m_V Z$ in a model with vectorlike fermions and $U(1)_X$ symmetry ($U(1)_X$VLFM), where m_V is a vector meson (ρ, ω, ϕ, J/ψ, Υ). The exotic Yukawa interactions in this model generate mixing between Standard Model (SM) fermions and vectorlike fermions, and this mixing affects the Higgs boson mass and Higgs couplings. The corrections to the CP-even and CP-odd $h\gamma Z$ couplings come from loop diagrams that involve the new particles, and these corrections have a clear impact on the decay rates of $h \to Z\gamma$ and $h \to m_V Z$. In suitable regions of the parameter space, the model can produce non-negligible deviations in $\Gamma_{\rm NP}(h \to Z\gamma)/\Gamma_{\rm SM}(h \to Z\gamma)$ and $\Gamma_{\rm NP}(h \to m_V Z)/\Gamma_{\rm SM}(h \to m_V Z)$, providing possible signals of new physics (NP) beyond the SM.

1 Introduction

In 2012, the ATLAS and CMS collaborations at the Large Hadron Collider (LHC) discovered a Higgs boson with a mass of about 125 GeV [1,2], clearly confirming that Electro-Weak (EW) Symmetry Breaking (EWSB) is realized through the Higgs mechanism. Within the current theoretical and experimental precision, its properties are consistent with the predictions of the Standard Model (SM). Although the SM has achieved great success in describing known particles and interactions, it still fails to address several important issues. In particular, if fermions obtain their masses solely through Yukawa interactions with the Higgs field, a pronounced hierarchy among fermion masses arises. For example, the mass ratio of the top quark to the electron reaches $m_t/m_e \approx 3.5 \times 10^5$, while neutrino masses m_ν lie only at the eV scale [3,4], leading to $m_t/m_\nu \approx 1.4 \times 10^{12}$ [5]. Furthermore, the SM contains no viable dark matter candidate, cannot explain the matter–antimatter asymmetry of the Universe, and does not resolve the hierarchy problem between the EW and Planck scales. These longstanding shortcomings motivate the exploration of possible extensions to the SM.

Therefore, a variety of representative theoretical frameworks beyond the SM have been proposed, including the Two-Higgs-Doublet Model (2HDM) [6,7], the Minimal Supersymmetric Standard Model (MSSM) and its extensions such as the NMSSM [8,9], as well as composite Higgs models in which the Higgs boson emerges as a composite pseudo-Nambu-Goldstone boson [10]. These extensions typically introduce additional scalar or fermionic degrees of freedom, making the Higgs interaction structure considerably richer than that of the SM. In many such models, new particles and interactions can induce flavor-changing or CP-violating Higgs couplings at tree level or loop level [6,11,12], thereby modifying the standard Higgs couplings and generating non-standard effective Higgs vertices. Specifically, although the SM forbids the $h\gamma Z$ vertex at tree level, it can be generated by loop contributions from new particles [13,14], thus becoming an important window for exploring new physics (NP).

In the SM, the decay of the Higgs boson into a Z boson and a photon ($h \to Z\gamma$) occurs through a loop diagram process, with a predicted branching ratio of approximately $\mathrm{BR}(h \to Z\gamma)=(1.5 \pm 0.1) \times 10^{-3}$ [15,16], which is similar in magnitude to $h \to \gamma\gamma$. Various extensions of the SM can alter this decay rate by introducing new particles into the loop diagram, making the ratio $\mathrm{BR}(h \to Z\gamma)/\mathrm{BR}(h \to \gamma\gamma)$ a sensitive probe for detecting NP effects. Additionally, the observation of $h \to Z\gamma$ can further confirm the coupling structure between the Higgs boson and the EW gauge bosons,

[a] e-mail: zhaosm@hbu.edu.cn (corresponding author)
[b] e-mail: dongxx@hbu.edu.cn

Published online: 14 June 2026

thereby deepening our understanding of the EWSB mechanism. Notably, this decay mode is also sensitive to potential anomalous trilinear Higgs self-couplings [17], and its precise measurement can help test the SM prediction of this fundamental quantity. Using proton-proton collision data at $\sqrt{s}$ = 13 TeV with an integrated luminosity of about 140 fb^{-1}, the ATLAS and CMS collaborations have recently reported the first evidence for this decay, with a combined statistical significance of 3.4σ. The measured signal strength is (2.2 ± 0.7) times the SM prediction, corresponding to a branching ratio of $(3.4 \pm 1.1) \times 10^{-3}$, which is consistent with theoretical expectations within 1.9σ [18].

The rare weak radiative Higgs decays $h \to m_V\gamma$ and $h \to m_V Z$, where m_V denotes a meson, have been extensively investigated in the literature [19–22]. Since the photon carries only transverse polarization, the decay $h \to m_V\gamma$ can produce only transversely polarized vector mesons. In contrast, in the $h \to m_V Z$ channel, the final state Z boson can be either longitudinally or transversely polarized, allowing both pseudoscalar and vector mesons to be generated. Depending on the decay topologies, the amplitude receives two types of contributions: a direct contribution, in which the Higgs couples directly to the quarks forming the meson, and an indirect contribution, where an off-shell electroweak gauge boson transitions into the meson through local matrix elements [23,24]. These two components exhibit substantial interference in the $h \to m_V\gamma$ channel [19–21]. For the $h \to m_V Z$ process, the indirect contribution induced by the effective $h\gamma Z$ vertex typically dominates over the direct one, particularly when m_V is a light vector meson [22]. Furthermore, QCD factorization has been applied to refine the theoretical description of $h \to m_V Z$ decays [25–28].

In recent years, experimental studies of Higgs boson decays into a Z boson and a vector meson have made steady progress. Although no evidence for these rare decay modes has been observed so far, current LHC measurements have already imposed stringent constraints on several channels. Using 137 fb^{-1} of proton-proton collision data collected at $\sqrt{s} = 13$ TeV, the CMS collaboration searched for a 125 GeV Higgs boson decaying into $Z\rho^0(770)$ and $Z\phi(1020)$. The resulting 95% confidence level (CL) upper limits on the branching ratios were found to be $1.04-1.31\%$ for $Z\rho^0$ and $0.31-0.40\%$ for $Z\phi$, corresponding to approximately 740–940 and 730–950 times their respective SM predictions [29]. CMS also reported a search for the decay $h \to ZJ/\psi$ using the same dataset, obtaining an upper limit of 1.9×10^{-3}, about 800 times the SM expectation [30]. While the current sensitivity remains far above the SM branching fractions, the experimental bounds on such rare Higgs decays continue to improve. With the forthcoming High-Luminosity LHC (HL-LHC), the prospects for probing these channels will be significantly enhanced, offering a promising opportunity to explore Higgs properties and potential NP effects.

Over the past decade, the absence of experimental evidence for supersymmetric particles has shifted considerable attention toward non-supersymmetric extensions of the SM. Among these possibilities, $U(1)_X$ frameworks containing vectorlike fermions provide a particularly economical and predictive class of models, capable of influencing both EW observables and flavor physics [31–35]. In the $U(1)_X$VLFM model considered in this work, one generation of vectorlike quarks, one generation of vectorlike leptons and two additional complex scalar fields are introduced, leading to a significantly richer phenomenology than that in the SM. A distinguishing feature of vectorlike fermions is that their left-handed and right-handed components carry identical SM gauge quantum numbers, allowing them to obtain gauge invariant masses without relying on EWSB [36]. Consequently, they do not generate sizable modifications to the Higgs production cross section, while still remaining accessible to direct searches at the LHC through their strong or EW production channels. Once vectorlike fermions mix with SM fermions, the couplings of the latter to the W, Z and Higgs bosons deviate from their SM forms [37]. This mixing not only violates the Glashow–Iliopoulos–Maiani (GIM) mechanism and induces tree-level flavor-changing neutral currents (FCNCs), but also introduces new sources of CP violation that can affect the electric dipole moments (EDMs) of leptons, quarks and neutrons [38]. Importantly, the model provides a natural explanation for the observed $b \to s\ell^+\ell^-$ anomalies, which indicate violation of lepton flavor universality (LFU). In this framework, the first two generations of SM fermions remain unchanged, while the third generation mixes with vectorlike fermions. This structure naturally modifies third-generation couplings while keeping the first two effectively SM-like, providing a minimal and theoretically motivated explanation for the anomalies. These features collectively highlight the theoretical and phenomenological significance of the $U(1)_X$VLFM model. Motivated by these considerations, we investigate the impact of this model on rare Higgs decay channels, focusing on $h \to Z\gamma$ and $h \to m_V Z$ with $m_V = \rho, \omega, \phi, J/\psi, \Upsilon$. Complementary analyses of $h \to \gamma\gamma$ and $h \to VV^*$ $(V = Z, W)$ are also presented. We derive the relevant Feynman rules and amplitudes, perform numerical parameter scans and identify regions of parameter space consistent with current experimental constraints.

The paper is organized as follows. In Sect. 2, we briefly introduce the main content of the $U(1)_X$VLFM. In Sect. 3, we present the analytical expressions of the Higgs boson decays $h \to Z\gamma$ and $h \to m_V Z$. The input parameters and numerical results are shown in Sect. 4. Our discussion and conclusion are given in Sect. 5. Finally, some mass matrices and couplings are collected in Appendix A, while Appendix B presents the explicit verification of anomaly cancellation in the $U(1)_X$VLFM model.

2 The $U(1)_X$VLFM

The gauge group of the $U(1)_X$VLFM is $SU(3)_C \otimes SU(2)_L \otimes U(1)_Y \otimes U(1)_X$, and the local gauge symmetries are broken through the Higgs mechanism. Compared with the SM, the model introduces three generations of right-handed neutrinos ν_R, two singlet Higgs fields ϕ and S, as well as one generation of vectorlike quarks, vectorlike leptons and vectorlike neutrino. The light neutrino masses are generated at the tree level via the seesaw mechanism [39–42]. The neutral CP-even components of the three scalar fields H, ϕ and S mix with each other, resulting in a 3×3 mass squared matrix. To obtain the 125 GeV Higgs boson mass, loop corrections should be taken into account. The $U(1)_X$ charges of all SM fields are assigned zero. The new fields beyond the SM are listed in Table 1.

There are one Higgs doublet and two Higgs singlets, whose specific forms are as follows:

$$H = \begin{pmatrix} H^0 \\ H^- \end{pmatrix}, \quad H^0 = \frac{1}{\sqrt{2}}\Big(v + \phi_H + i\sigma_H\Big), \tag{1}$$

$$\phi = \frac{1}{\sqrt{2}}\Big(v_P + \phi_P + i\sigma_P\Big), \quad S = \frac{1}{\sqrt{2}}\Big(v_S + \phi_S + i\sigma_S\Big). \tag{2}$$

In Eqs. (1–2), v, v_P and v_S denote the nonzero vacuum expectation values (VEVs) corresponding to the Higgs superfields H, ϕ and S, respectively.

The relevant Lagrangian of the $U(1)_X$VLFM reads as

$$\begin{aligned}
\mathcal{L} = {} & \mu_H^2 H^\dagger H + \mu_P^2 |\phi|^2 + \mu_X^2 |S|^2 - \lambda_H (H^\dagger H)^2 \\
& - \lambda_P |\phi|^4 - \lambda_X |S|^4 - \lambda_{HP} (H^\dagger H)|\phi|^2 \\
& - \lambda_{HX} (H^\dagger H)|S|^2 - \lambda_{PX} |S|^2 |\phi|^2 + S d^*_{XL,k} Y^*_{XD,jk} d_{R,j} \\
& + S u^*_{R,j} Y_{XU,jk} u_{XL,k} + S e^*_{XL,k} Y^*_{XE,jk} e_{R,j} \\
& + S \nu^*_{R,j} Y_{XN,jk} \nu_{XL,k} + \phi d^*_{XL,k} Y^*_{PD,jk} d_{XR,j} \\
& + \phi u^*_{XR,j} Y_{PU,jk} u_{XL,k} + \phi e^*_{XL,k} Y^*_{PE,jk} e_{XR,j} \\
& + \phi \nu^*_{XR,j} Y_{PN,jk} \nu_{XL,k} + Y^*_{u,jk} \bar{q}_{L,k} H u_{R,j} \\
& - Y^*_{d,jk} \bar{q}_{L,k} \tilde{H} d_{R,j} - Y^*_{e,jk} \bar{l}_k \tilde{H} e_{R,j} + h.c.
\end{aligned} \tag{3}$$

We denote the $U(1)_Y$ charge by Y^Y and the $U(1)_X$ charge by Y^X. As discussed in the textbook [43], the SM is anomaly free. For the $U(1)_X$VLFM model considered here, the cancellation of gauge and gravitational anomalies can be summarized as follows:

1. The anomalies involving three $SU(2)_L$ gauge bosons vanish exactly as in the SM, and the same applies to the corresponding $SU(3)_C$ anomaly.
2. The anomalies with one $SU(3)_C$ or one $SU(2)_L$ gauge boson are proportional to $\mathrm{Tr}[t^a] = 0$ or $\mathrm{Tr}[\tau^a] = 0$, respectively, and therefore vanish.
3. The mixed anomalies involving one $U(1)_Y$ or $U(1)_X$ and two $SU(3)_C$ gauge bosons are proportional to

$$\begin{aligned}
\mathrm{Tr}[t^a t^b Y^Y] &= \frac{1}{2}\delta^{ab} \sum_q Y^Y_q, \\
\mathrm{Tr}[t^a t^b Y^X] &= \frac{1}{2}\delta^{ab} \sum_q Y^X_q.
\end{aligned} \tag{4}$$

4. Similarly, the anomalies containing one $U(1)_Y$ or $U(1)_X$ boson and two $SU(2)_L$ bosons are proportional to

$$\begin{aligned}
\mathrm{Tr}[\tau^a \tau^b Y^Y] &= \frac{1}{2}\delta^{ab} \sum_L Y^Y_L, \\
\mathrm{Tr}[\tau^a \tau^b Y^X] &= \frac{1}{2}\delta^{ab} \sum_L Y^X_L.
\end{aligned} \tag{5}$$

5. The anomalies of the three $U(1)$ gauge bosons are classified into four types

$$\begin{aligned}
&\mathrm{Tr}[Y^Y Y^Y Y^Y] = \sum_n (Y^Y_n)^3, \quad \mathrm{Tr}[Y^X Y^X Y^X] = \sum_n (Y^X_n)^3, \\
&\mathrm{Tr}[Y^X Y^Y Y^Y] = \sum_n Y^X_n (Y^Y_n)^2, \\
&\mathrm{Tr}[Y^Y Y^X Y^X] = \sum_n Y^Y_n (Y^X_n)^2.
\end{aligned} \tag{6}$$

6. The gravitational anomaly with one $U(1)_Y$ or $U(1)_X$ gauge boson is proportional to

$$\mathrm{Tr}[Y^Y] = \sum_n Y^Y_n, \quad \mathrm{Tr}[Y^X] = \sum_n Y^X_n. \tag{7}$$

For the parts that do not involve $U(1)_X$, the anomaly conditions are identical to those in the SM and can be easily verified to vanish. The cancellation of the $U(1)_X$ anomalies is also ensured, even though their structure is considerably more intricate than that of the SM. The explicit derivation of all $U(1)_X$-related anomalies is presented in Appendix B. Therefore, the $U(1)_X$VLFM model is anomaly free.

In the $U(1)_X$VLFM model, the coexistence of the two Abelian gauge groups $U(1)_Y$ and $U(1)_X$ leads to a new effect absent in the SM: gauge kinetic mixing. As discussed in Ref. [45], a kinetic mixing term between Abelian gauge fields can generally appear in the Lagrangian without violating gauge invariance. In models containing more than one $U(1)$ gauge group, the Abelian gauge interactions can be written in a matrix form and the gauge fields can be redefined by a rotation in gauge space [44]. Moreover, even if the kinetic mixing term is set to zero at a certain scale, it can generally be radiatively generated at low energies through renormalization group (RG) evolution [45].

Table 1 Properties of new particles introduced in the model

Field	$SU(3)_C$	$SU(2)_L$	$U(1)_Y$	$U(1)_X$
ϕ	1	1	0	$Q_a + Q_b$
S	1	1	0	Q_a
ν_R	1	1	0	0
d_{XL}	3	1	$-1/3$	Q_a
u_{XL}	3	1	$2/3$	$-Q_a$
d_{XR}	$\bar{3}$	1	$1/3$	Q_b
u_{XR}	$\bar{3}$	1	$-2/3$	$-Q_b$
e_{XL}	1	1	-1	Q_a
ν_{XL}	1	1	0	$-Q_a$
e_{XR}	1	1	1	Q_b
ν_{XR}	1	1	0	$-Q_b$

The covariant derivative of this model can be written in the general form

$$D_\mu = \partial_\mu - i \left(Y^Y,\ Y^X \right) \begin{pmatrix} g_Y, & g'_{YX} \\ g'_{XY}, & g'_X \end{pmatrix} \begin{pmatrix} A'^Y_\mu \\ A'^X_\mu \end{pmatrix}, \tag{8}$$

where A'^Y_μ and A'^X_μ denote the gauge fields of $U(1)_Y$ and $U(1)_X$, respectively. The Abelian gauge fields can be redefined by a rotation in gauge space using an orthogonal matrix R ($R^T R = 1$) [44,45], yielding

$$\begin{pmatrix} g_Y, & g'_{YX} \\ g'_{XY}, & g'_X \end{pmatrix} R^T = \begin{pmatrix} g_1, & g_{YX} \\ 0, & g_X \end{pmatrix}, \tag{9}$$

which redefines the $U(1)$ gauge fields as

$$R \begin{pmatrix} A'^Y_\mu \\ A'^X_\mu \end{pmatrix} = \begin{pmatrix} A^Y_\mu \\ A^X_\mu \end{pmatrix}. \tag{10}$$

g_X denotes the gauge coupling constant associated with the $U(1)_X$ symmetry, while g_{YX} characterizes the gauge kinetic mixing between the $U(1)_Y$ and $U(1)_X$ gauge groups. The neutral gauge bosons A^Y_μ, V^3_μ and A^X_μ mix together at the tree level, leading to the mass matrix in the $(A^Y_\mu, V^3_\mu, A^X_\mu)$ basis

$$\begin{pmatrix} \frac{1}{4}g_1^2 v^2 & -\frac{1}{4}g_1 g_2 v^2 & \frac{1}{4}g_1 g_{YX} v^2 \\ -\frac{1}{4}g_1 g_2 v^2 & \frac{1}{4}g_2^2 v^2 & -\frac{1}{4}g_2 g_{YX} v^2 \\ \frac{1}{4}g_1 g_{YX} v^2 & -\frac{1}{4}g_2 g_{YX} v^2 & \frac{1}{4}g_{YX}^2 v^2 + \frac{1}{4}g_X^2 \xi^2 \end{pmatrix} \tag{11}$$

with $\xi^2 = 4(Q_a + Q_b)^2 v_P^2 + 4Q_a^2 v_S^2$.

To diagonalize the mass matrix in Eq. (11), we use a unitary transformation involving two mixing angles θ_W and θ'_W

$$\begin{pmatrix} \gamma_\mu \\ Z_\mu \\ Z'_\mu \end{pmatrix} = \begin{pmatrix} \cos\theta_W & \sin\theta_W & 0 \\ -\sin\theta_W \cos\theta'_W & \cos\theta_W \cos\theta'_W & \sin\theta'_W \\ \sin\theta_W \sin\theta'_W & -\cos\theta'_W \sin\theta'_W & \cos\theta'_W \end{pmatrix} \begin{pmatrix} A^Y_\mu \\ V^3_\mu \\ A^X_\mu \end{pmatrix}. \tag{12}$$

The additional mixing angle θ'_W appears in the couplings involving Z and Z', and is given by

$$\sin^2\theta'_W = \frac{1}{2} - \frac{(g_{YX}^2 - g_1^2 - g_2^2)v^2 + g_X^2\xi^2}{2\sqrt{(g_{YX}^2 + g_1^2 + g_2^2)^2 v^4 + 2g_X^2(g_{YX}^2 - g_1^2 - g_2^2)v^2\xi^2 + g_X^4\xi^4}}. \tag{13}$$

Under the physical condition that $v \ll v_P, v_S$, we can introduce a small parameter $\epsilon' = v^2/\xi^2 \ll 1$. Using a first-order approximation, the formula can be simplified to:

$$\theta'_W \simeq \frac{|g_{YX}|\sqrt{g_1^2 + g_2^2}}{g_X^2} \frac{v^2}{\xi^2}. \tag{14}$$

Substituting typical model parameters ($g_1 = \frac{e}{\cos\theta_W}$, $g_2 = \frac{e}{\sin\theta_W}$, $g_X = 0.6$, $g_{YX} = -0.1$, $Q_a = Q_b = 1$, $v_P = 4500$ GeV, $v_S = 8500$ GeV, $v = 246$ GeV), we obtain $\theta'_W \sim 2 \times 10^{-5}$.

The exact mass eigenvalues in Eq. (11) are

$$\begin{aligned} m_\gamma^2 &= 0, \\ m_{Z,Z'}^2 &= \frac{1}{8}\Big((g_1^2 + g_2^2 + g_{YX}^2)v^2 + g_X^2\xi^2 \\ &\quad \mp \sqrt{[(g_1^2 + g_2^2 + g_{YX}^2)v^2 + g_X^2\xi^2]^2 - 4(g_1^2 + g_2^2)g_X^2 v^2 \xi^2}\Big). \end{aligned} \tag{15}$$

The simplified Higgs potential is given by

$$\begin{aligned} V = &-\mu_H^2 H^\dagger H - \mu_P^2 |\phi|^2 - \mu_X^2 |S|^2 + \lambda_H (H^\dagger H)^2 \\ &+ \lambda_P |\phi|^4 + \lambda_X |S|^4 + \lambda_{HP}(H^\dagger H)|\phi|^2 \\ &+ \lambda_{HX}(H^\dagger H)|S|^2 + \lambda_{PX}|S|^2|\phi|^2. \end{aligned} \tag{16}$$

The VEVs of the Higgs fields should satisfy the following equations

$$2\lambda_H v^2 - 2\mu_H^2 + \lambda_{HP} v_P^2 + \lambda_{HX} v_S^2 = 0, \tag{17}$$

$$2\lambda_X v_S^2 - 2\mu_X^2 + \lambda_{HX} v^2 + \lambda_{PX} v_P^2 = 0, \tag{18}$$

$$2\lambda_P v_P^2 - 2\mu_P^2 + \lambda_{HP} v^2 + \lambda_{PX} v_S^2 = 0. \tag{19}$$

In the (ϕ_H, ϕ_S, ϕ_P) basis, the CP-even Higgs mass squared matrix is

$$m_h^2 = \begin{pmatrix} m_{\phi_H\phi_H} & -\lambda_{HX} v v_S & -\lambda_{HP} v v_P \\ -\lambda_{HX} v v_S & m_{\phi_S\phi_S} & -\lambda_{PX} v_P v_S \\ -\lambda_{HP} v v_P & -\lambda_{PX} v_P v_S & m_{\phi_P\phi_P} \end{pmatrix}, \tag{20}$$

$$m_{\phi_H\phi_H} = \frac{1}{2}\Big(-6\lambda_H v^2 - \lambda_{HP} v_P^2 - \lambda_{HX} v_S^2 \Big) + \mu_H^2, \tag{21}$$

$$m_{\phi_S\phi_S} = \frac{1}{2}\Big(-6\lambda_X v_S^2 - \lambda_{HX} v^2 - \lambda_{PX} v_P^2 \Big) + \mu_X^2, \tag{22}$$

$$m_{\phi_P\phi_P} = \frac{1}{2}\Big(-6\lambda_P v_P^2 - \lambda_{HP} v^2 - \lambda_{PX} v_S^2 \Big) + \mu_P^2. \tag{23}$$

This matrix is diagonalized by Z^H

$$Z^H m_h^2 Z^{H,\dagger} = m_{2,h}^{dia}, \tag{24}$$

with

$$\phi_H = \sum_j Z_{j1}^H h_j, \quad \phi_S = \sum_j Z_{j2}^H h_j, \quad \phi_P = \sum_j Z_{j3}^H h_j. \tag{25}$$

The mass squared matrix for the CP-odd Higgs bosons in the basis $(\sigma_H, \sigma_S, \sigma_P)$ is diagonalized by Z^A via the relation $Z^A m_{A_h}^2 Z^{A,\dagger} = m_{2,A_h}^{dia}$. After imposing the tadpole conditions (Eqs. 17–19), the full CP-odd mass matrix takes the form:

$$m_{A_h}^2 = \begin{pmatrix} m_{\sigma_H\sigma_H} & m_{\sigma_S\sigma_H} & m_{\sigma_P\sigma_H} \\ m_{\sigma_H\sigma_S} & m_{\sigma_S\sigma_S} & m_{\sigma_P\sigma_S} \\ m_{\sigma_H\sigma_P} & m_{\sigma_S\sigma_P} & m_{\sigma_P\sigma_P} \end{pmatrix}, \tag{26}$$

with

$$m_{\sigma_H\sigma_H} = \frac{1}{4}\kappa v^2 \Big(g_{YX}\cos\theta'_W + \big(g_2\cos\theta_W + g_1\sin\theta_W\big) \sin\theta'_W \Big)^2, \tag{27}$$

$$m_{\sigma_H\sigma_S} = -\frac{1}{2}\kappa g_X Q_a v v_S \cos\theta'_W \Big(g_{YX}\cos\theta'_W + \big(g_2\cos\theta_W + g_1\sin\theta_W\big)\sin\theta'_W \Big), \tag{28}$$

$$m_{\sigma_S\sigma_S} = \kappa g_X^2 Q_a^2 v_S^2 \cos^2\theta'_W, \tag{29}$$

$$m_{\sigma_H\sigma_P} = -\frac{1}{2}\kappa g_X (Q_a + Q_b) v v_P \cos\theta'_W \Big(g_{YX}\cos\theta'_W + \big(g_2\cos\theta_W + g_1\sin\theta_W\big)\sin\theta'_W \Big), \tag{30}$$

$$m_{\sigma_S\sigma_P} = \kappa g_X^2 Q_a (Q_a + Q_b) v_P v_S \cos^2\theta'_W, \tag{31}$$

$$m_{\sigma_P\sigma_P} = \kappa g_X^2 (Q_a + Q_b)^2 v_P^2 \cos^2\theta'_W. \tag{32}$$

Here

$$\sigma_H = \sum_j Z_{j1}^A A_{h,j}, \ \sigma_S = \sum_j Z_{j2}^A A_{h,j}, \ \sigma_P = \sum_j Z_{j3}^A A_{h,j}. \tag{33}$$

Diagonalizing this matrix, one finds that the CP-odd sector contains a single massive state and two Goldstone bosons, which are eaten by the SM Z and the Z'. The physical, massive CP-odd state, denoted by A, has mass

$$\begin{aligned} m_A^2 = \frac{1}{16}\kappa \Big\{ & (g_1^2 + 2g_{YX}^2 + g_2^2) v^2 + 2 g_X^2 \xi^2 \\ & + \Big(2 g_X^2 \xi^2 - (g_1^2 - 2g_{YX}^2 + g_2^2) v^2 \Big) \cos 2\theta'_W \\ & + 2v^2 \Big[\Big((-g_1^2 + g_2^2)\cos 2\theta_W + 2 g_1 g_2 \sin 2\theta_W \Big) \sin^2\theta'_W \\ & + 2 g_{YX} (g_2 \cos\theta_W + g_1 \sin\theta_W) \sin 2\theta'_W \Big] \Big\}. \end{aligned} \tag{34}$$

The physical field A is an admixture of the pseudoscalar component σ_H of the SM Higgs and the pseudoscalar components σ_S and σ_P:

$$A = \frac{-\epsilon\sigma_H + 2r\sigma_S + 2\sigma_P}{\sqrt{4 + 4r^2 + \epsilon^2}}, \tag{35}$$

with

$$\begin{aligned} \epsilon &= \frac{v(g_{YX} + g_2\cos\theta_W \tan\theta'_W + g_1 \sin\theta_W \tan\theta'_W)}{g_X v_P (Q_a + Q_b)\cos\theta'_W}, \\ r &= \frac{Q_a v_S}{(Q_a + Q_b) v_P}. \end{aligned} \tag{36}$$

The two Goldstone modes, which are orthogonal to A, are given by linear combinations of the remaining fields:

$$\begin{aligned} G_Z^0 &= \cos\theta'_W G_1 - \sin\theta'_W G_2, \\ G_{Z'}^0 &= \sin\theta'_W G_1 + \cos\theta'_W G_2, \end{aligned} \tag{37}$$

where

$$\begin{aligned} G_1 &= \frac{2\alpha\sigma_H + \sigma_P}{\sqrt{1 + 4\alpha^2}}, \\ G_2 &= \frac{2\beta\sigma_H + (1 + 4\alpha^2)\sigma_S - 4\alpha\beta\sigma_P}{\sqrt{(1 + 4\alpha^2)(1 + 4\alpha^2 + 4\beta^2)}}, \end{aligned} \tag{38}$$

$$\alpha = \frac{g_X v_P (Q_a + Q_b)\cos\theta'_W}{v\Big(g_{YX}\cos\theta'_W + (g_2\cos\theta_W + g_1\sin\theta_W)\sin\theta'_W \Big)}, \tag{39}$$

$$\beta = \frac{g_X v_S Q_a \cos\theta'_W}{v\Big(g_{YX}\cos\theta'_W + (g_2\cos\theta_W + g_1\sin\theta_W)\sin\theta'_W \Big)}$$

The mixing angle θ'_W is given by Eq. (13). In the relevant parameter space of the model, the $Z - Z'$ mixing angle satisfies $\theta'_W \sim 10^{-5}$, so that $\cos\theta'_W \approx 1$ and $\sin\theta'_W \ll 1$. In this limit, one can approximate $G_Z^0 \approx G_1$ and $G_{Z'}^0 \approx G_2$. Furthermore, since $v_P, v_S \gg v$, we have $|\alpha|, |\beta| \gg 1$, which clearly shows that G_Z^0 is primarily composed of σ_H, while $G_{Z'}^0$ is primarily an admixture of σ_S and σ_P. This is consistent with the physical expectation that the Goldstone modes are eaten by the SM Z and the Z' bosons.

The down-type quark mass matrix in the (d_L, d_{XL}) and (d_R^*, d_{XR}^*) basis is given by

$$m_d = \begin{pmatrix} \frac{1}{\sqrt{2}} v Y_d^T & 0 \\ \frac{1}{\sqrt{2}} v_S Y_{XD}^T & \frac{1}{\sqrt{2}} v_P Y_{PD}^T \end{pmatrix}, \tag{40}$$

which is diagonalized by U_L^d and U_R^d according to

$$U_L^{d,*}\, m_d\, U_R^{d,\dagger} = m_d^{dia}. \tag{41}$$

Furthermore, the mass matrices for the up-type quark and lepton are derived in the same way and listed in the Appendix A.

We now introduce the couplings needed in this model, and begin by presenting some interactions involving the Z boson. In the below equations, $P_L = \frac{1-\gamma_5}{2}$ and $P_R = \frac{1+\gamma_5}{2}$.

$$\begin{aligned}
\mathcal{L}_{Z\bar{e}_i e_j} &= \bar{e}_i \Big\{ \frac{i}{2} \Big[\Big(-g_1 \cos\theta'_W \sin\theta_W + g_2 \cos\theta_W \cos\theta'_W \\
&\quad + g_{YX} \sin\theta'_W \Big) \sum_{a=1}^{3} U^{e,*}_{L,ja} U^{e}_{L,ia} \\
&\quad + 2 \Big((-g_X Q_a + g_{YX}) \sin\theta'_W \\
&\quad - g_1 \cos\theta'_W \sin\theta_W \Big) U^{e,*}_{L,j4} U^{e}_{L,i4} \Big] \gamma_\mu P_L \\
&\quad + i \Big[\Big(g_{YX} \sin\theta'_W \\
&\quad - g_1 \cos\theta'_W \sin\theta_W \Big) \sum_{a=1}^{3} U^{e,*}_{R,ia} U^{e}_{R,ja} \\
&\quad + \Big((g_X Q_b + g_{YX}) \sin\theta'_W \\
&\quad - g_1 \cos\theta'_W \sin\theta_W \Big) U^{e,*}_{R,i4} U^{e}_{R,j4} \Big] \gamma_\mu P_R \Big\} e_j Z_\mu, \qquad (42) \\
\mathcal{L}_{Z\bar{d}_i d_j} &= \bar{d}_i \Big\{ \frac{i}{6} \Big[\Big(3g_2 \cos\theta_W \cos\theta'_W + g_1 \cos\theta'_W \sin\theta_W \\
&\quad - g_{YX} \sin\theta'_W \Big) \sum_{a=1}^{3} U^{d,*}_{L,ja} U^{d}_{L,ia} \\
&\quad + 2 \Big((-3g_X Q_a + g_{YX}) \sin\theta'_W \\
&\quad - g_1 \cos\theta'_W \sin\theta_W \Big) U^{d,*}_{L,j4} U^{d}_{L,i4} \Big] \gamma_\mu P_L \\
&\quad + \frac{i}{3} \Big[\Big(g_{YX} \sin\theta'_W \\
&\quad - g_1 \cos\theta'_W \sin\theta_W \Big) \sum_{a=1}^{3} U^{d,*}_{R,ia} U^{d}_{R,ja} \\
&\quad + \Big((3g_X Q_b + g_{YX}) \sin\theta'_W \\
&\quad - g_1 \cos\theta'_W \sin\theta_W \Big) U^{d,*}_{R,i4} U^{d}_{R,j4} \Big] \gamma_\mu P_R \Big\} d_j Z_\mu. \qquad (43)
\end{aligned}$$

To save space in the text, the remaining vertices employed in our calculation are compiled in the Appendix A.

3 The processes $h \to Z\gamma$ and $h \to m_V Z$

This section provides the analytical expressions for the decay $h \to Z\gamma$ and the weak hadronic Higgs decay $h \to m_V Z$. The representative Feynman diagrams of the process $h \to m_V Z$ are shown in Fig. 1. Figure 1a, b correspond to the direct contributions, while Fig. 1c, d denote the indirect ones. In loop induced topologies, the effective vertex $h \to Z\gamma^*$ is represented by a crossed circle. As discussed in Ref. [22], the direct contributions originate from the coupling between the Higgs boson and the constituent quarks of the final state vector meson. Although these diagrams appear at tree level, they usually give only a subdominant contribution. The indirect contributions proceed through the decay process $h \to ZZ^*/Z\gamma^* \to m_V Z$, where the off-shell bosons Z^* or γ^* hadronize into the vector meson. In the topology of Fig. 1c, the virtual Z can in principle be replaced by a Z'. However, current limits require $m_{Z'} > 5.15$ TeV, making its effect negligible. Numerically, $|\frac{1}{m_V^2 - m_Z^2}| \sim \frac{1}{90^2\ \text{GeV}^2}$ and $|\frac{1}{m_V^2 - m_{Z'}^2}| \sim \frac{1}{5100^2\ \text{GeV}^2}$, indicating that the latter is approximately 10^{-4} times the former; therefore the Z' exchange is omitted in our analysis. Among the indirect contributions, the decay $h \to ZZ^*$ occurs at tree level in the SM, while the $h\gamma Z$ interaction is loop induced. In the $U(1)_X$VLFM framework, this vertex receives additional nonstandard contributions. The corresponding effective Lagrangian is given by

$$\begin{aligned}
\mathcal{L}_{eff} = \frac{\alpha}{4\pi v} \Big(& \frac{2C_{\gamma Z}}{\sin\theta_W \cos\theta_W} h F_{\mu v} Z^{\mu v} \\
& - \frac{2\tilde{C}_{\gamma Z}}{\sin\theta_W \cos\theta_W} h F_{\mu v} \tilde{Z}^{\mu v} \Big). \qquad (44)
\end{aligned}$$

Here, θ_W is the weak mixing angle. Using the effective Lagrangian in Eq. (44), the decay width of $h \to Z\gamma$ is derived

$$\begin{aligned}
\Gamma(h \to Z\gamma) = & \frac{\alpha^2 m_h^3}{32\pi^3 v^2 \sin^2\theta_W \cos^2\theta_W} \left(1 - \frac{m_Z^2}{m_h^2}\right)^3 \\
& (|C_{\gamma Z}|^2 + |\tilde{C}_{\gamma Z}|^2). \qquad (45)
\end{aligned}$$

Loop diagrams associated with NP can induce additional corrections to the processes $h \to m_V\gamma$ and $h \to m_V Z$. Although these decays share similar topologies, their physical properties differ significantly. In the case of $h \to m_V\gamma$, the photon in the final state is on shell and massless, and therefore does not possess a longitudinal polarization component. Within the NRQCD framework, the gauge invariant amplitude for $h \to m_V\gamma$ at tree level can be written as

$$\begin{aligned}
\mathcal{M}^\gamma = & \frac{4\sqrt{3} e e_q \phi_0}{m_h^2 - m_V^2} \left(\frac{m_V G_F}{2\sqrt{2}}\right)^{\frac{1}{2}} \Big[c_S \{ 2(\varepsilon_\gamma^* \cdot p_V)(\varepsilon_V^* \cdot k_\gamma) - (m_h^2 \\
& - m_V^2)(\varepsilon_\gamma^* \cdot \varepsilon_V^*) \} - 2 c_P \epsilon_{\mu v \rho \lambda}\, \varepsilon_\gamma^{*\mu} k_\gamma^\nu p_V^\rho \varepsilon_V^{*\lambda} \Big]. \qquad (46)
\end{aligned}$$

Here, $k_\gamma (p_V)$ denotes the four-momentum of the photon (vector meson), and $\varepsilon_\gamma^* (\varepsilon_V^*)$ is the corresponding polarization vector.

In the rest frame of the vector meson, Eq. (46) can be recast into a more transparent form. Using the definitions

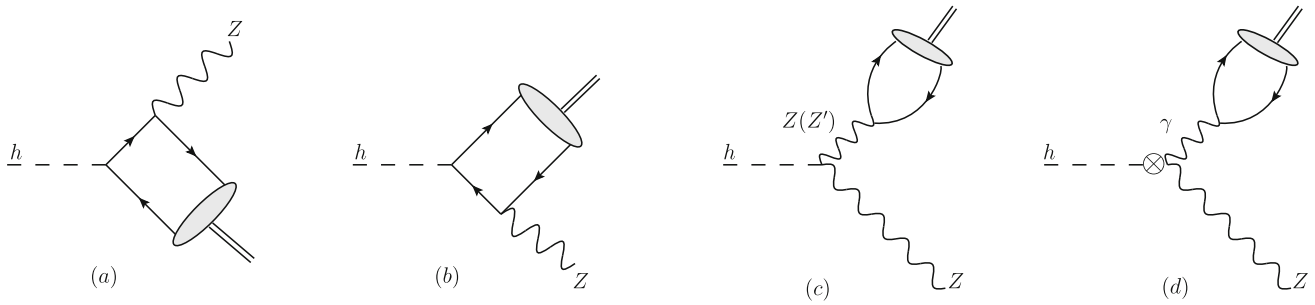

Fig. 1 The diagrams contributing to the decay $h \to m_V Z$

$\varepsilon_V^{*L} \equiv \bar{\varepsilon}_V^* \cdot \hat{k}_\gamma$ and $\bar{\varepsilon}_V^{*T} \equiv \bar{\varepsilon}_V^* - \varepsilon_V^{*L}\hat{k}_\gamma$, the decay amplitude in the transverse basis becomes [46]

$$\mathcal{M}^\gamma = H_\parallel^\gamma \vec{\varepsilon}_V^{*T} \cdot \vec{\varepsilon}_\gamma^* + i H_\perp^\gamma \hat{k}_\gamma \cdot (\vec{\varepsilon}_V^{*T} \times \vec{\varepsilon}_\gamma^*), \tag{47}$$

$$H_\parallel^\gamma = 4\sqrt{3} e e_q \phi_0 \Big(\frac{m_V G_F}{2\sqrt{2}}\Big)^{\frac{1}{2}} c_S, \tag{48}$$

$$H_\perp^\gamma = 4\sqrt{3} e e_q \phi_0 \Big(\frac{m_V G_F}{2\sqrt{2}}\Big)^{\frac{1}{2}} i c_P. \tag{49}$$

Because the photon in the final state is both massless and on shell, longitudinal polarization does not contribute to the amplitude and only transverse polarizations appear in Eq. (47). The triple product $\hat{k}_\gamma \cdot (\vec{\varepsilon}_V^{*T} \times \vec{\varepsilon}_\gamma^*)$ constitutes the unique P-odd observable in $|\mathcal{M}|^2$, whose coefficient is proportional to $c_S c_P$. The parameter c_P encodes a pseudoscalar $Hq\bar{q}$ coupling arising from possible NP effects and manifests itself through a nonzero value of this triple product. However, since the photon does not decay, its polarization cannot be reconstructed experimentally, making a direct measurement of c_P impossible.

To overcome the limitation imposed by the unobservable photon polarization, one may instead consider replacing the photon with a massive vector boson Z, whose polarization can be measured through its decay. Unlike the photon, the Z boson couples to the Higgs already at tree level, introducing an additional diagram that contributes to the decay $h \to m_V Z$. Although the $Z\bar{q}q$ interaction contains an axial-vector component, this term does not contribute to the leading NRQCD matrix element for $h \to m_V Z$. In the rest frame of the vector meson, we choose $\hat{k}_Z$ as the direction of the outgoing Z boson. Following an analysis analogous to the $h \to m_V \gamma$ case, the decay amplitude can be written in the transverse-longitudinal basis as

$$\mathcal{M}^Z = H_0^Z \vec{\varepsilon}_V^{*L} \cdot \vec{\varepsilon}_Z^{*L} + H_\parallel^Z \vec{\varepsilon}_V^{*T} \cdot \vec{\varepsilon}_Z^{*T} + i H_\perp^Z \hat{k}_Z \cdot (\vec{\varepsilon}_V^{*T} \times \vec{\varepsilon}_Z^{*T}). \tag{50}$$

The coefficients H_0^Z and $H_\parallel^Z$ scale with the scalar coupling c_S, while $H_\perp^Z$ is proportional to the pseudoscalar parameter c_P. Explicit expressions for these form factors can be found in Ref. [46]. Since the polarization of the Z boson can be inferred from its decay products, the transverse component ε_Z^{*T} is experimentally accessible. A nonvanishing triple-product term would therefore constitute clear evidence for a pseudoscalar contribution and provide a direct probe of c_P.

For the decay $h \to m_V Z$, the amplitude is commonly expressed in terms of longitudinal and transverse polarization components. A convenient parametrization reads

$$i\mathcal{A}(h \to m_V Z) = -\frac{2 g m_V}{\cos\theta_W v}\Bigg[\varepsilon_V^{\parallel *} \cdot \varepsilon_Z^{\parallel *} F_\parallel^{VZ} + \varepsilon_V^{\perp *} \cdot \varepsilon_Z^{\perp *} F_\perp^{VZ} + \frac{\epsilon_{\mu\nu\alpha\beta} k_V^\mu k_Z^\nu \varepsilon_V^{*\alpha} \varepsilon_Z^{*\beta}}{\Big[(k_V \cdot k_Z)^2 - k_V^2 k_Z^2\Big]^{1/2}} \tilde{F}_\perp^{VZ}\Bigg],$$

where k_Z is the four-momentum of the outgoing Z boson. The longitudinal and transverse polarization vectors of the vector meson are defined by [22]

$$\varepsilon_V^{\parallel\mu} = \frac{1}{m_V} \frac{k_V \cdot k_Z}{\Big[(k_V \cdot k_Z)^2 - k_V^2 k_Z^2\Big]^{1/2}} \left(k_V^\mu - \frac{k_V^2}{k_V \cdot k_Z} k_Z^\mu\right),$$
$$\varepsilon_V^{\perp\mu} = \varepsilon_V^\mu - \varepsilon_V^{\parallel\mu}. \tag{52}$$

The polarization vectors of the Z boson follow from Eq. (52) by performing the replacements $m_V \to m_Z$ and $k_V \leftrightarrow k_Z$.

For the decay $h \to m_V Z$, the partial width can be written as

$$\Gamma(h \to m_V Z) = \frac{m_h^3}{4\pi v^4} \lambda^{1/2}(1, r_Z, r_V)(1 - r_Z - r_V)^2 \times \Big[|F_\parallel^{VZ}|^2 + \frac{8 r_Z r_V}{(1 - r_Z - r_V)^2}(|F_\perp^{VZ}|^2 + |\tilde{F}_\perp^{VZ}|^2)\Big], \tag{53}$$

where $\lambda(x, y, z) = (x - y - z)^2 - 4yz$, $r_Z = m_Z^2/m_h^2$ and $r_V = m_V^2/m_h^2$. Although $r_V \ll 1$ for light vector mesons, the transverse amplitudes exhibit a notable sensitivity to this small parameter. To avoid losing such effects, we retain $r_V = m_V^2/m_h^2$ rather than employing a massless approximation, which leads to a more accurate description of the transverse polarization contributions.

In Eq. (53), the three form factors $F_\parallel^{VZ}$, $F_\perp^{VZ}$ and $\tilde{F}_\perp^{VZ}$ each receive contributions from both direct and indirect

mechanisms. For convenience, we first present the indirect parts, which arise from the effective $h\gamma Z$ vertex and the tree-level hZZ coupling, and their expressions are given as follows

$$
\begin{aligned}
F^{VZ}_{\parallel\,\text{indirect}} &= \frac{\kappa_Z}{1-r_V/r_Z}\sum_q f_V^q\, v_q \\
&\quad + C_{\gamma Z}\,\frac{\alpha(m_V)}{4\pi}\,\frac{4r_Z}{1-r_Z-r_V}\sum_q f_V^q\, Q_q, \\
F^{VZ}_{\perp\,\text{indirect}} &= \frac{\kappa_Z}{1-r_V/r_Z}\sum_q f_V^q\, v_q \\
&\quad + C_{\gamma Z}\,\frac{\alpha(m_V)}{4\pi}\,\frac{1-r_Z-r_V}{r_V}\sum_q f_V^q\, Q_q, \\
\widetilde{F}^{VZ}_{\perp\,\text{indirect}} &= \widetilde{C}_{\gamma Z}\,\frac{\alpha(m_V)}{4\pi}\,\frac{\lambda^{1/2}(1,r_Z,r_V)}{r_V}\sum_q f_V^q\, Q_q. \qquad (54)
\end{aligned}
$$

The vector and axial-vector couplings of $Z\bar{q}q$ are expressed as $v_q = \frac{T_3^q}{2} - Q_q \sin^2\theta_W$ and $a_q = \frac{T_3^q}{2}$, respectively. The vector meson decay constant f_V^q is introduced through

$$
\left\langle V(k,\varepsilon)|\bar{q}\gamma^\mu q|0\right\rangle = -if_V^q m_V \varepsilon^{*\mu}, \quad q = u,d,s\ldots \qquad (55)
$$

To calculate the results, we make use of the relations

$$
Q_V f_V = \sum_q Q_q f_V^q, \quad \sum_q f_V^q v_q = f_V v_V. \qquad (56)
$$

The specific forms of $C_{\gamma Z}$ and $\tilde{C}_{\gamma Z}$ in Eq. (54) are as follows [47]

$$
\begin{aligned}
C_{\gamma Z} &= C_{\gamma Z}^{SM,light} + C_{\gamma Z}^{U(1)_X},\ \tilde{C}_{\gamma Z} = \tilde{C}_{\gamma Z}^{SM,light} + \tilde{C}_{\gamma Z}^{U(1)_X}, \\
C_{\gamma Z}^{SM,light} &= \sum_{q=u,d,c,s}\frac{2N_c Q_q v_q}{3}A_f(\tau_q,r_Z) \\
&\quad + \sum_{l=\mu,e}\frac{2Q_l v_l}{3}A_f(\tau_l,r_Z) - \frac{1}{2}A_W^{\gamma Z}(\tau_W,r_Z), \\
\tilde{C}_{\gamma Z}^{SM,light} &= \sum_{q=u,d,c,s}\tilde{\kappa}_q N_c Q_q v_q B_f(\tau_q,r_Z) \\
&\quad + \sum_{l=\mu,e}\tilde{\kappa}_l Q_l v_l B_f(\tau_l,r_Z), \qquad (57)
\end{aligned}
$$

with $\tau_i = 4m_i^2/m_h^2$. $C_{\gamma Z}^{SM,light}$ and $\tilde{C}_{\gamma Z}^{SM,light}$ correspond to the first two generation SM fermions and W gauge boson contributions to $h \to Z\gamma$, while A_f, B_f and $A_W^{\gamma Z}$ are all loop functions [19–21].

Figure 2 shows the NP one loop corrections to the decay $h \to Z\gamma$ in the $U(1)_X$VLFM model. The new contributions to $C_{\gamma Z}$ arise mainly from the vectorlike leptons and vectorlike quarks introduced in the model. The mixing between the vectorlike fermions and the third generation SM fermions induces additional effects in the fermionic loop amplitudes, rendering them different from the purely SM contributions. As noted in Ref. [48], the QCD corrections to the $h \to Z\gamma$ decay width are at the level of about 0.1%, which is extremely small and can be safely neglected in our analysis.

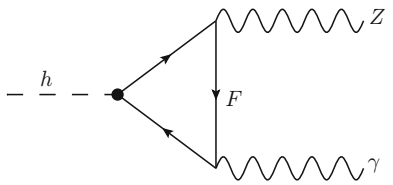

Fig. 2 The one loop diagrams with new particles for the decay $h \to Z\gamma$

The extended gauge structure modifies the effective couplings that enter the fermionic loop amplitudes. To illustrate this explicitly, we take the $Z - \bar{u}_i - u_i$ vertex as an example. The corresponding interactions in the SM and $U(1)_X$VLFM are given by

$$
\begin{aligned}
\mathcal{L}^{SM}_{Z\bar{u}u} &= \bar{u}_i\Big\{-\frac{e}{2\sin\theta_W\cos\theta_W}\Big(1-\frac{4}{3}\sin^2\theta_W\Big)\gamma_\mu P_L \\
&\quad + \frac{2e\sin\theta_W}{3\cos\theta_W}\gamma_\mu P_R\Big\}u_i Z_\mu, \qquad (58) \\
\mathcal{L}^{U(1)_X}_{Z\bar{u}u} &= \bar{u}_i\Big\{-\frac{i}{6}\Big[\Big(3g_2\cos\theta_W\cos\theta'_W - g_1\cos\theta'_W\sin\theta_W \\
&\quad + g_{YX}\sin\theta'_W\Big)\sum_{a=1}^{3}U^{u,*}_{L,ja}U^{u}_{L,ia} \\
&\quad + 2\Big((2g_{YX}-3g_X Q_a)\sin\theta'_W 2g_1\cos\theta'_W\sin\theta_W\Big) \\
&\quad U^{u,*}_{L,j4}U^{u}_{L,i4}\Big]\gamma_\mu P_L \\
&\quad + \frac{i}{3}\Big[2\Big(g_1\cos\theta'_W\sin\theta_W - g_{YX}\sin\theta'_W\Big) \\
&\quad \sum_{a=1}^{3}U^{u,*}_{R,ia}U^{u}_{R,ja} \\
&\quad + \Big(2g_1\cos\theta'_W\sin\theta_W - (3g_X Q_b + 2g_{YX})\sin\theta'_W\Big) \\
&\quad U^{u,*}_{R,i4}U^{u}_{R,j4}\Big]\gamma_\mu P_R\Big\}u_j Z_\mu, \qquad (59)
\end{aligned}
$$

where the couplings in Eq. (59) depend on θ'_W, g_X and g_{YX}, with θ'_W originating from the Z-Z' mixing.

Setting $\theta'_W = 0$ and assuming no mixing between the three SM up-type quarks and the vectorlike fourth generation, Eq. (59) reduces to

$$
\begin{aligned}
\mathcal{L}^{U(1)_X}_{Z\bar{u}u} &\to \frac{1}{6}\bar{u}_i\Big[(-3g_2\cos\theta_W + g_1\sin\theta_W)\gamma_\mu P_L \\
&\quad + 4g_1\sin\theta_W\gamma_\mu P_R\Big]u_i Z^\mu \\
&= \bar{u}_i\Big[-\frac{e}{2\sin\theta_W\cos\theta_W}\Big(1-\frac{4}{3}\sin^2\theta_W\Big)\gamma_\mu P_L \\
&\quad + \frac{2e\sin\theta_W}{3\cos\theta_W}\gamma_\mu P_R\Big]u_i Z^\mu. \qquad (60)
\end{aligned}
$$

which is identical to the SM result in Eq. (58).

Our numerical analysis shows that the typical value of the mixing angle is $\theta'_W \sim 10^{-5}$ in the $U(1)_X$VLFM, leading to a relative deviation $\frac{\mathcal{L}^{SM}_{Z\bar{u}u}-\mathcal{L}^{U(1)_X}_{Z\bar{u}u}}{\mathcal{L}^{SM}_{Z\bar{u}u}}$ is at the order of 10^{-5}. Such a tiny difference has a negligible impact on the loop induced amplitudes. Therefore, for fermionic loops involving SM fields, we safely adopt the SM couplings in our calculations.

In the $U(1)_X$VLFM, the CP-even coupling $C^{U(1)_X}_{\gamma Z}$ reads

$$
\begin{aligned}
C^{U(1)_X}_{\gamma Z} &= \frac{v\sin\theta_W\cos\theta_W}{e}\int_0^1 dx\int_0^1 ydy \sum_{F=t,b,\tau,t',b',\tau'} \\
&\Bigg[\frac{Q_{F1}}{R^2_{1N}(m_{F_1},m_{F_2})}\Big(A^{\bar{F}_2F_1h}B^{\bar{F}_1F_2Z}\times(-2(x-1)y^2 \\
&(m_{F_1}+m_{F_2})+y(2x(m_{F_1}+m_{F_2})-3m_{F_1} \\
&-m_{F_2})+m_{F_1})+A^{\bar{F}_2F_1h}_w B^{\bar{F}_1F_2Z}_w(m_{F_1}(y-1) \\
&(2(x-1)y+1)+ym_{F_2} \\
&(-2xy+2x+2y-1))\Big)+\frac{Q_{F1}}{R^2_{2N}(m_{F_1},m_{F_2})} \\
&\Big(A^{\bar{F}_2F_1h}B^{\bar{F}_1F_2Z}(-2(x-1)y^2(m_{F_1}+m_{F_2}) \\
&+y(x-1)\times(3m_{F_1}+m_{F_2})+m_{F_1}) \\
&+A^{\bar{F}_2F_1h}_w B^{\bar{F}_1F_2Z}_w(m_{F_1}(y-1) \\
&(2(x-1)y+1) \\
&-y(m_{F_1}x+m_{F_2}(x-1)(2y-1)))\Big)\Bigg]. \qquad (61)
\end{aligned}
$$

The explicit expression of $C^{U(1)_X}_{\gamma Z}$ is given by

$$
\begin{aligned}
\tilde{C}^{U(1)_X}_{\gamma Z} &= -\frac{iv\sin\theta_W\cos\theta_W}{e}\int_0^1 dx\int_0^1 ydy \\
&\sum_{F=t,b,\tau,t',b',\tau'}\Bigg[\frac{1}{R^2_{1N}(m_{F_1},m_{F_2})} \\
&\times\Big(A^{\bar{F}_2F_1h}B^{\bar{F}_1F_2Z}_w(y(m_{F_1}+m_{F_2})-m_{F_1}) \\
&+A^{\bar{F}_2F_1h}_w B^{\bar{F}_1F_2Z}(m_{F_1}(1-y)+m_{F_2}y)\Big) \\
&+\frac{1}{R^2_{2N}(m_{F_1},m_{F_2})} \\
&\Big(A^{\bar{F}_2F_1h}B^{\bar{F}_1F_2Z}_w(y(1-x)(m_{F_1}+m_{F_2})-m_{F_1}) \\
&+A^{\bar{F}_2F_1h}_w B^{\bar{F}_1F_2Z}\times((x-1)y(m_{F_1} \\
&-m_{F_2})+m_{F_1})\Big)\Bigg]. \qquad (62)
\end{aligned}
$$

The functions $R^2_{1N}(m_1,m_2)$ and $R^2_{2N}(m_1,m_2)$ are shown as

$$
\begin{aligned}
R^2_{1N}(m_1,m_2) &= p_2^2(1-x)^2y^2+p_1^2(1-y)^2-2p_1\cdot p_2(1-x) \\
&\quad y(1-y)+m_2^2xy+(m_2^2-p_2^2)(1-x)y \\
&\quad +(m_1^2-p_1^2)(1-y), \\
R^2_{2N}(m_1,m_2) &= p_1^2(1-x)^2y^2+p_2^2(1-y)^2-2p_1\cdot p_2(1-x) \\
&\quad y(1-y)+m_2^2xy+(m_2^2-p_1^2)(1-x)y \\
&\quad +(m_1^2-p_2^2)(1-y). \qquad (63)
\end{aligned}
$$

The interaction between F_1, F_2, and the Higgs boson is parametrized by the scalar and pseudoscalar couplings $A^{\bar{F}_2F_1h}$ and $A^{\bar{F}_2F_1h}_w$. The Z-boson couplings to $\bar{F}_1F_2$ are encoded in the vector and axial-vector coefficients $B^{\bar{F}_1F_2Z}$ and $B^{\bar{F}_1F_2Z}_w$. These interactions can be written in the generic form

$$
\begin{aligned}
&\bar{F}_2 i(A^{\bar{F}_2F_1h}+A^{\bar{F}_2F_1h}_w\gamma_5)F_1h,\ \bar{F}_1 i(B^{\bar{F}_1F_2Z}\gamma_\mu \\
&+B^{\bar{F}_1F_2Z}_w\gamma_\mu\gamma_5)F_2Z^\mu. \qquad (64)
\end{aligned}
$$

All explicit expressions for the relevant vertices are provided in Sect. 2 and Appendix A.

The direct and indirect contributions behave very differently: the former can only be evaluated as an expansion in power series of $(m_q/m_h)^2$ or $(\Lambda_{QCD}/m_h)^2$, where m_q denotes the constituent quark mass inside the meson and Λ_{QCD} characterizes the hadronic scale. For a longitudinally polarized vector meson, the direct contribution originates from subleading-twist components and is therefore power suppressed. In contrast, for a transversely polarized vector meson, the leading-twist distribution amplitude enters directly. Using the asymptotic form $\phi_V^\perp(x)=6x(1-x)$ [49–51], the direct contributions take the form

$$
F^{VZ}_{\perp\,\text{direct}} = \sum_q f_V^{q\perp}v_q\,\kappa_q\,\frac{3m_q}{2m_V}\,\frac{1-r_Z^2+2r_Z\ln r_Z}{(1-r_Z)^2}, \qquad (65)
$$

$$
\widetilde{F}^{VZ}_{\perp,\text{direct}} = \sum_q f_V^{q\perp}v_q\,\tilde{\kappa}_q\,\frac{3m_q}{2m_V}\,\frac{1-r_Z^2+2r_Z\ln r_Z}{(1-r_Z)^2}. \qquad (66)
$$

Although these expressions may appear numerically comparable to the indirect term in Eq. (54), the direct contributions remain strongly suppressed once the small quark masses are taken into account. The main reason is that the relevant vertices originate from Yukawa interactions. In the $U(1)_X$VLFM model studied in this work, the Yukawa couplings between fermions and Higgs are given by $Y_{u_i}=\sqrt{2}\,m_{u_i}/v$, $Y_{d_i}=\sqrt{2}\,m_{d_i}/v$, $Y_{e_i}=\sqrt{2}\,m_{l_i}/v$, where $v=246\,\text{GeV}$ is the electroweak vacuum expectation value. Therefore, the strength of the corresponding vertices is proportional to the fermion masses. As a result, smaller quark masses lead to weaker couplings, which significantly suppresses the direct contributions.

For vector mesons composed of light quarks, such as ρ, ω, ϕ, the dominant constituents are u, d and s quarks, whose masses are approximately $m_u, m_d \sim \mathcal{O}(\text{MeV})$, $m_s \sim 0.1\,\text{GeV}$. Consequently, the corresponding Yukawa couplings are of the order $Y_{u,d} \sim 10^{-5}$, $Y_s \sim 10^{-3}$. These values are strongly suppressed compared with typical electroweak couplings. Therefore, the direct contributions in processes dominated by these light quarks can be safely neglected.

For vector mesons composed of heavy quarks, such as $J/\psi(c\bar{c})$ and $\Upsilon(b\bar{b})$, the corresponding quark masses are approximately $m_c \sim 1.3\,\text{GeV}$, $m_b \sim 4.2\,\text{GeV}$. This leads to $Y_c \sim 10^{-2}$, $Y_b \sim 10^{-2}$. Although these values are larger than those for light quarks, they remain significantly smaller than typical electroweak couplings. Therefore, even for heavy quarkonia such as J/ψ and Υ, the direct contributions are relatively enhanced but still remain subleading, while the indirect contributions considered in this work dominate the processes.

4 Numerical analysis

In this section, we impose several experimental constraints on the parameter space of the $U(1)_X$VLFM:

1. The mass of the lightest CP-even Higgs boson is fixed to $m_h = 125.20 \pm 0.11$ GeV [5].
2. After mixing between the third-generation SM fermions and the vectorlike states, the physical masses are required to reproduce the SM values: $m_t = 172.57 \pm 0.29\,\text{GeV}$, $m_b = 4.183 \pm 0.007\,\text{GeV}$, $m_\tau = 1.78 \pm 0.09\,\text{GeV}$ [5].
3. The latest ATLAS and CMS results set 95% CL lower mass bounds of about 1.49−1.52 TeV for vectorlike quarks [52]. For vectorlike leptons, CMS excludes long-lived scenarios below 700 GeV [53], while ATLAS electroweak searches exclude masses below 910 GeV [54].
4. The additional gauge boson satisfies $M_{Z'} \geq 5.15\,\text{TeV}$ at 95% CL [55]. Moreover, the ratio $\frac{M_{Z'}}{g_X}$ is constrained to be larger than 6 TeV at 99% CL [56,57], which limits the gauge coupling to $0 < g_X \leq 0.85$.

After applying these experimental requirements, a sizable set of viable sample points is obtained, from which one-dimensional distributions and multidimensional scatter plots are constructed.

The numerical analysis is organized into four parts: (1) determination of the relevant input parameters; (2) analysis of the decays $h \to \gamma\gamma$ and $h \to VV^*(V = Z, W)$; (3) discussion of the $h \to Z\gamma$ decay; (4) study of the processes $h \to m_V Z$, where $m_V = \omega, \rho, \phi, J/\psi, \Upsilon$.

4.1 The input parameters scheme

Under the constraints from quark and charged-lepton masses, the Yukawa couplings for the first two generations are taken as

$$\begin{aligned} &Y_{u_i} = \sqrt{2}\, m_{u_i}/v, \qquad Y_{d_i} = \sqrt{2}\, m_{d_i}/v, \\ &Y_{e_i} = \sqrt{2}\, m_{l_i}/v \quad (i = 1, 2), \end{aligned} \tag{67}$$

while the third-generation Yukawa couplings are determined by the mixing with the vectorlike fermions, given by

$$\begin{aligned} Y_{u_3} &= \frac{\sqrt{2}\, m_t \sqrt{2m_t^2 - v_P^2 Y_{PU}^2 - v_S^2 Y_{XU}^2}}{v\sqrt{2m_t^2 - v_P^2 Y_{PU}^2}}, \\ Y_{d_3} &= \frac{\sqrt{2}\, m_b \sqrt{2m_b^2 - v_P^2 Y_{PD}^2 - v_S^2 Y_{XD}^2}}{v\sqrt{2m_b^2 - v_P^2 Y_{PD}^2}}, \\ Y_{e_3} &= \frac{\sqrt{2}\, m_\tau \sqrt{2m_\tau^2 - v_P^2 Y_{PE}^2 - v_S^2 Y_{XE}^2}}{v\sqrt{2m_\tau^2 - v_P^2 Y_{PE}^2}}. \end{aligned} \tag{68}$$

Here m_{u_i}, m_{d_i} and m_{l_i} denote the up-type quark, down-type quark and charged-lepton masses, respectively, and their values are taken from the latest PDG [5].

The following model parameters are fixed throughout the analysis

$$\begin{aligned} &Q_a{=}1, \quad Q_b{=}1, \quad \lambda_H{=}0.14, \quad \lambda_P{=}0.1, \quad \lambda_X = 0.06, \\ &\lambda_{HP} = 0.01, \quad \lambda_{HX} = 0.05, \quad \lambda_{PX} = 0.05. \end{aligned} \tag{69}$$

For the numerical study, we scan over the parameter set

$$\begin{aligned} &g_X, \quad g_{YX}, \quad Y_{XD}, \quad Y_{PD}, \quad Y_{XU}, \\ &Y_{PU}, \quad Y_{XE}, \quad Y_{PE}, \quad v_P, \quad v_S, \end{aligned} \tag{70}$$

which contains the dominant inputs affecting the predictions of $h \to Z\gamma$ and $h \to m_V Z$ in the $U(1)_X$VLFM.

In addition, the numerical inputs for the vector meson decay parameters, including m_V, f_V, v_V, Q_V and the ratio $f_V^\perp/f_V = f_V^{q\perp}/f_V^q$, are compiled in Table 2. Here, $f_V^\perp$ and $f_V^{q\perp}$ denote the transverse decay constants and the flavor-specific transverse decay constants, respectively.

4.2 The processes $h \to \gamma\gamma$ and $h \to VV^*$

In this section, under the parameter choice $g_X = 0.6$, $g_{YX} = -0.1$, $Y_{XE} = 0.5$, $Y_{PE} = 0.005$, $v_P = 4500\,\text{GeV}$, $v_S = 8500\,\text{GeV}$, we evaluate the ratios $R_{\gamma\gamma}$ and $R_{VV^*}(V = Z, W)$ corresponding to the decay processes $h \to \gamma\gamma$ and $h \to VV^*$, respectively.

Setting $Y_{XU} = 0.5$ and $Y_{PU} = 0.07$, Fig. 3 illustrates how $R_{\gamma\gamma}$ varies as a function of Y_{XD}. The black, red, blue and green curves correspond to $Y_{PD} = 0.005$, $Y_{PD} =$

Table 2 Input values for the vector meson decay constants

Vector meson	ω	ρ	ϕ	J/ψ	Υ
m_V/GeV	0.782	0.77	1.02	3.097	9.46
f_V/GeV	0.194	0.216	0.223	0.403	0.684
υ_V	$-\frac{\sin^2\theta_W}{3\sqrt{2}}$	$\frac{1}{\sqrt{2}}(\frac{1}{2}-\sin^2\theta_W)$	$-\frac{1}{4}+\frac{\sin^2\theta_W}{3}$	$\frac{1}{4}-\frac{2\sin^2\theta_W}{3}$	$-\frac{1}{4}+\frac{\sin^2\theta_W}{3}$
Q_V	$\frac{1}{3\sqrt{2}}$	$\frac{1}{\sqrt{2}}$	$-\frac{1}{3}$	$\frac{2}{3}$	$-\frac{1}{3}$
$f_V^\perp/f_V = f_V^{q\perp}/f_V^q$	0.71	0.72	0.76	0.91	1.09

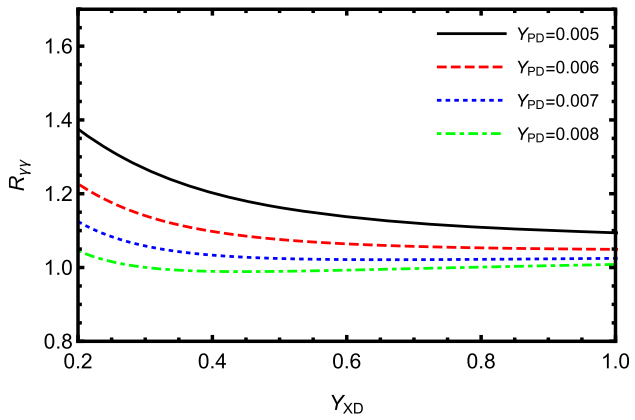

Fig. 3 $R_{\gamma\gamma}$ varying with Y_{XD} for different Y_{PD}

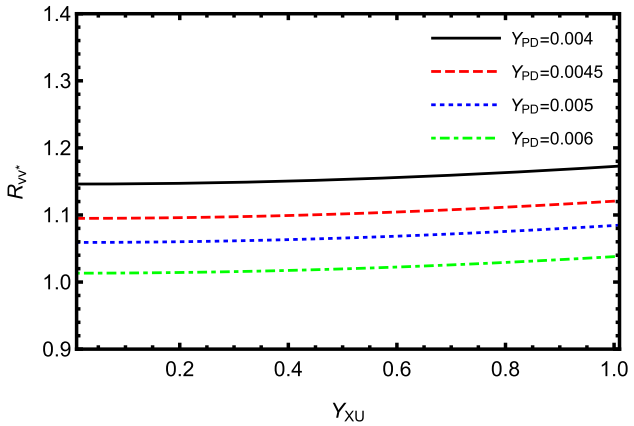

Fig. 4 R_{VV^*} varying with Y_{XU} for different Y_{PD}

0.006, $Y_{PD} = 0.007$ and $Y_{PD} = 0.008$, respectively. As observed in the Fig. 3, all four curves exhibit a mildly decreasing trend as Y_{XD} increases, and they gradually level off at larger values of Y_{XD}. Moreover, increasing Y_{PD} systematically lowers the overall height of the curves. In the small Y_{XD} region, especially for smaller Y_{PD} the predicted values of $R_{\gamma\gamma}$ are generally above the experimental central value. As Y_{XD} increases, however, all four curves gradually decrease and converge toward the vicinity of 1.1, leading to improved agreement between the theoretical predictions and the experimental measurement.

Based on the inputs $Y_{XD} = 0.5$ and $Y_{PU} = 0.055$, the black ($Y_{PD} = 0.004$), red ($Y_{PD} = 0.0045$), blue ($Y_{PD} = 0.005$) and green ($Y_{PD} = 0.006$) curves in Fig. 4 present the dependence of R_{VV^*} on Y_{XU}. Overall, all four curves exhibit a mild upward trend: as Y_{XU} increases, R_{VV^*} rises gradually and monotonically, with a very small slope. This indicates that the impact of Y_{XU} on this ratio is positive but relatively weak. In addition, smaller values of Y_{PD} shift the entire curve upward. The four curves are nearly parallel and show only minimal fluctuations throughout the plotted range, with their values confined to the narrow interval of approximately 1.03−1.15.

Since the parameter choices satisfy the Higgs experimental constraints, we no longer display the results for $R_{\gamma\gamma}$ and $R_{VV^*}(V = Z, W)$ in the subsequent numerical analysis.

4.3 The process $h \to Z\gamma$

The NP contribution to the decay $h \to m_V Z$ originates from the effective $hZ\gamma$ coupling. Therefore, investigating the $h \to Z\gamma$ process is crucial for probing the properties of the Higgs boson. According to the latest experimental results, the signal strength is measured to be $\mu_{Z\gamma} = 2.2 \pm 0.7$ [18]. For the numerical evaluation of the $h \to Z\gamma$ decay width, we adopt the parameter set $Y_{XD} = 0.8$, $Y_{PD} = 0.01$, $Y_{XE} = 0.5$, $Y_{PE} = 0.01$, $\upsilon_P = 4500$ GeV, $\upsilon_S = 8500$ GeV, and perform $\Gamma_{NP}(h \to Z\gamma)/\Gamma_{SM}(h \to Z\gamma)$ schematic diagrams affected by different parameters in the Figs. 5 and 6.

Figure 5 is obtained using the parameter ranges listed in Table 3. We classify the numerical results in the Y_{PU} and Y_{XU} plane using ▲ ($\Gamma_{NP}(h \to Z\gamma)/\Gamma_{SM}(h \to Z\gamma) < 1.294$), ■ ($1.294 \le \Gamma_{NP}(h \to Z\gamma)/\Gamma_{SM}(h \to Z\gamma) < 1.3$), ♦ ($1.3 \le \Gamma_{NP}(h \to Z\gamma)/\Gamma_{SM}(h \to Z\gamma) < 1.35$) and • ($1.35 \le \Gamma_{NP}(h \to Z\gamma)/\Gamma_{SM}(h \to Z\gamma)$. Here, Y_{XU} and Y_{PU} denote the Yukawa couplings between the SM-like and vector-like up-type quarks. Specifically, Y_{XU} couples the SM right-handed quark u_R to the vector-like left-handed quark u_{XL}, whereas Y_{PU} represents the coupling between the left-hand and right-handed components of the vector-like quarks u_{XL} and u_{XR}. As shown in Fig. 5, a substantial portion of the parameter space leads to a significant deviation

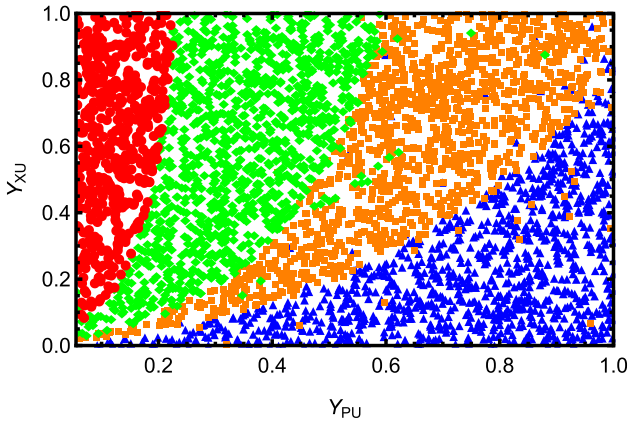

Fig. 5 $\Gamma_{NP}(h \to Z\gamma)/\Gamma_{SM}(h \to Z\gamma)$ in $Y_{PU} - Y_{XU}$ plane, and the marking of the scattering points represents: ▲ ($\Gamma_{NP}(h \to Z\gamma)/\Gamma_{SM}(h \to Z\gamma) < 1.294$), ■ ($1.294 \leq \Gamma_{NP}(h \to Z\gamma)/\Gamma_{SM}(h \to Z\gamma) < 1.3$), ♦ ($1.3 \leq \Gamma_{NP}(h \to Z\gamma)/\Gamma_{SM}(h \to Z\gamma) < 1.35$), • ($1.35 \leq \Gamma_{NP}(h \to Z\gamma)/\Gamma_{SM}(h \to Z\gamma)$

of $\Gamma_{NP}(h \to Z\gamma)/\Gamma_{SM}(h \to Z\gamma)$ from the SM prediction. In particular, when Y_{PU} is small or Y_{XU} is in the moderate to high range, the red and green regions become dominant, indicating that the ratio can be enhanced to 1.30–1.35 or even higher. This corresponds to a deviation of about 30–35%, far exceeding the theoretical uncertainties within the SM. In contrast, the regions close to the SM prediction (blue points) are mainly confined to the lower right corner of the plane, where Y_{PU} is relatively large and Y_{XU} remains small.

Fixing the parameters at Y_{PU}=0.075 and Y_{XU}=1, we further plot in Fig. 6 the dependence of $\Gamma_{NP}(h \to Z\gamma)/\Gamma_{SM}(h \to Z\gamma)$ on g_X. Here g_X denotes the gauge coupling constant of the $U(1)_X$ group, while g_{YX} represents the gauge kinetic mixing between $U(1)_Y$ and $U(1)_X$. As shown in Fig. 6, the ratio $\Gamma_{NP}(h \to Z\gamma)/\Gamma_{SM}(h \to Z\gamma)$ is nearly independent of g_X and remains around 1.65 for all considered values of g_{YX}, corresponding to an enhancement of approximately 65% over the SM prediction.

4.4 The processes $h \to m_V Z$

In this section, we analyze the decay processes $h \to m_V Z$. The decay constants of the vector mesons ω, ρ, J/ψ, ϕ, Υ are listed in Table 2.

Table 3 Scanning parameters for Fig. 5

Parameters	Min	Max
g_X	0.05	0.85
g_{YX}	−0.7	0.7
Y_{PU}	0.055	1
Y_{XU}	0	1

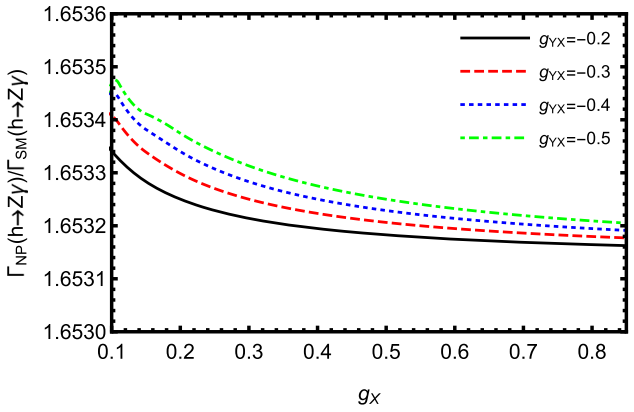

Fig. 6 $\Gamma_{NP}(h \to Z\gamma)/\Gamma_{SM}(h \to Z\gamma)$ varying with g_X for different g_{YX}

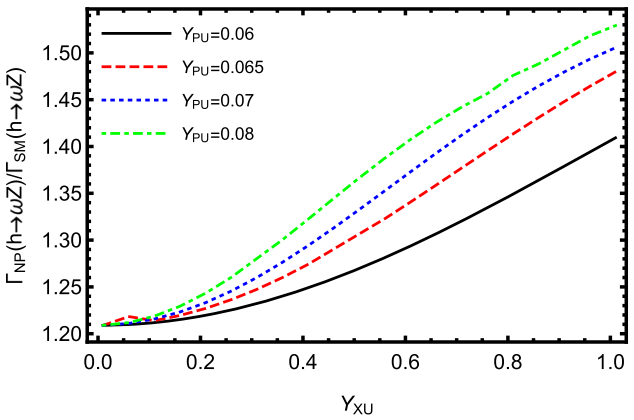

Fig. 7 $\Gamma_{NP}(h \to \omega Z)/\Gamma_{SM}(h \to \omega Z)$ varying with Y_{XU} for different Y_{PU}

Table 4 Scanning parameters for Fig. 8

Parameters	Min	Max
g_X	0.05	0.85
g_{YX}	−0.7	0.7
Y_{PD}	−1	1
Y_{XD}	−1	1

4.4.1 The process $h \to \omega Z$

At first, we study the decay $h \to \omega Z$ and some suppositions are taken as $Y_{XE} = 0.5$, $Y_{PE} = 0.01$, $v_P = 4500$ GeV, $v_S = 8500$ GeV.

For the parameter choice $g_X = 0.6$, $g_{YX} = -0.1$, $Y_{XD} = 0.8$, $Y_{PD} = 0.01$, $\Gamma_{NP}(h \to \omega Z)/\Gamma_{SM}(h \to \omega Z)$ versus Y_{XU} is shown in Fig. 7. As can be seen, all four curves exhibit a monotonic increase from left to right, with the larger value of Y_{PU} (the green line corresponding to Y_{PU}=0.08) lying above the others throughout the entire parameter range. The ratio always exceeds 1.2 across all parameter variations, and

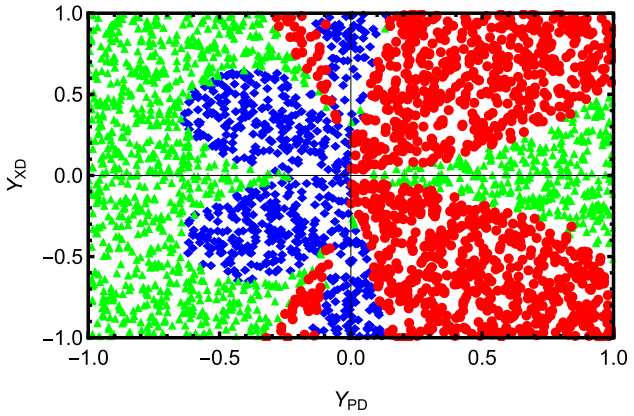

Fig. 8 $\Gamma_{NP}(h \to \omega Z)/\Gamma_{SM}(h \to \omega Z)$ in $Y_{PD} - Y_{XD}$ plane, and the marking of the scattering points represents: ♦ $(\Gamma_{NP}(h \to \omega Z)/\Gamma_{SM}(h \to \omega Z) < 1.58)$, ▲ $(1.58 \leq \Gamma_{NP}(h \to \omega Z)/\Gamma_{SM}(h \to \omega Z) < 1.6)$, ● $(1.6 \leq \Gamma_{NP}(h \to \omega Z)/\Gamma_{SM}(h \to \omega Z)$

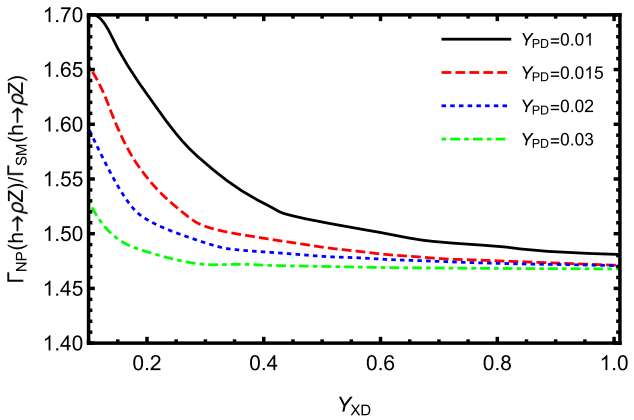

Fig. 9 $\Gamma_{NP}(h \to \rho Z)/\Gamma_{SM}(h \to \rho Z)$ varying with Y_{XD} for different Y_{PD}

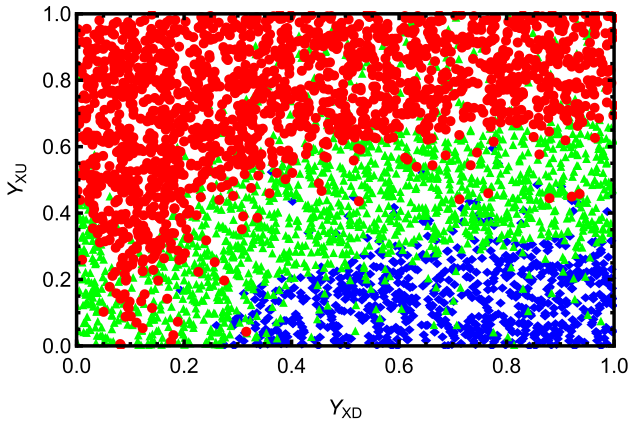

Fig. 10 $\Gamma_{NP}(h \to \rho Z)/\Gamma_{SM}(h \to \rho Z)$ in $Y_{XD} - Y_{XU}$ plane, and the marking of the scattering points represents: ♦ $(\Gamma_{NP}(h \to \rho Z)/\Gamma_{SM}(h \to \rho Z) < 1.26)$, ▲ $(1.26 \leq \Gamma_{NP}(h \to \rho Z)/\Gamma_{SM}(h \to \rho Z) < 1.4)$, ● $(1.4 \leq \Gamma_{NP}(h \to \rho Z)/\Gamma_{SM}(h \to \rho Z)$

it can reach 1.45−1.50 around $Y_{XU} \approx 1$, corresponding to a sizable enhancement of about 20–50% relative to the SM prediction.

To further investigate the decay $h \to \omega Z$ and identify the regions of viable parameter space, we study the effects of the parameters g_X, g_{YX}, Y_{PD}, Y_{XD}. We generate a scatter plot in the (Y_{PD}, Y_{XD}) plane under the condition $Y_{XU} = 1$, $Y_{PU} = 0.075$. Using the parameter ranges given in Table 4, the resulting distribution is shown in Fig. 8. The scatter points are categorized as ♦ for $\Gamma_{NP}(h \to \omega Z)/\Gamma_{SM}(h \to \omega Z) < 1.58$, ▲ for $1.58 \leq \Gamma_{NP}(h \to \omega Z)/\Gamma_{SM}(h \to \omega Z) < 1.6$ and ● for $1.6 \leq \Gamma_{NP}(h \to \omega Z)/\Gamma_{SM}(h \to \omega Z)$. The parameter Y_{XD} controls the mixing between the vector-like down-type quarks and the third-generation SM quarks, while Y_{PD} mainly determines the mass of the vector-like down-type quarks. It is evident that the parameter space exhibits an approximately symmetric distribution with respect to the horizontal axis. The blue region with a smaller ratio (< 1.58) is confined to a narrow area slightly left of the center of the plot. Surrounding it is the green region with moderately larger values (1.58−1.60). Most notably, the vast majority of the parameter space, particularly regions with $Y_{PD} > 0$ or $|Y_{XD}| > 0.3$, is entirely dominated by red scatter points, corresponding to $\Gamma_{NP}(h \to \omega Z)/\Gamma_{SM}(h \to \omega Z) \geq 1.6$. This indicates that in these regions the decay width exceeds the SM prediction by at least 60%.

4.4.2 *The process* $h \to \rho Z$

Secondly, we analyze the numerical results for the decay process $h \to \rho Z$ and set the parameters $g_X = 0.6$, $g_{YX} = -0.1$, $Y_{PU} = 0.075$, $Y_{PE} = 0.01$, $v_P = 4500$ GeV, $v_S = 8500$ GeV.

Assuming $Y_{XU} = 1$, $Y_{XE} = 0.5$, the variation of the ratio $\Gamma_{NP}(h \to \rho Z)/\Gamma_{SM}(h \to \rho Z)$ with Y_{XD} is presented in Fig. 9, where the black, red, blue and green curves correspond to $Y_{PD} = 0.01,\ 0.015,\ 0.02,\ 0.03$, respectively. Over the entire scanning range $Y_{XD} \in [0.1,\ 1.0]$, the four curves lie significantly above unity, resulting in a deviation of approximately 45–70% from the SM prediction. All curves exhibit a peak in the region of small Y_{XD}, with the Y_{PD}=0.01 curve reaching the largest value, around 1.70. As Y_{XD} increases, the curves show a decreasing trend and gradually approach a stable behavior, eventually converging to the interval of about 1.48−1.50 for $Y_{XD} \gtrsim 0.6$. Moreover, smaller values of Y_{PD} correspond to a higher overall curve.

To further explore the multidimensional behavior of the sensitive parameters, we fix $Y_{PD} = 0.01$ and generate Fig. 10 by sampling points according to Table 5, illustrating the behavior of the $h \to \rho Z$ decay rate as a function of Y_{XD} and Y_{XU}. The parameter plane is clearly divided

Table 5 Scanning parameters for Fig. 10

Parameters	Min	Max
Y_{XD}	0	1
Y_{XU}	0	1
Y_{XE}	0	1

Table 6 Scanning parameters for Fig. 11

Parameters	Min	Max
g_X	0.05	0.85
g_{YX}	−0.7	0.7
Y_{PE}	0	1
Y_{XE}	−1	1

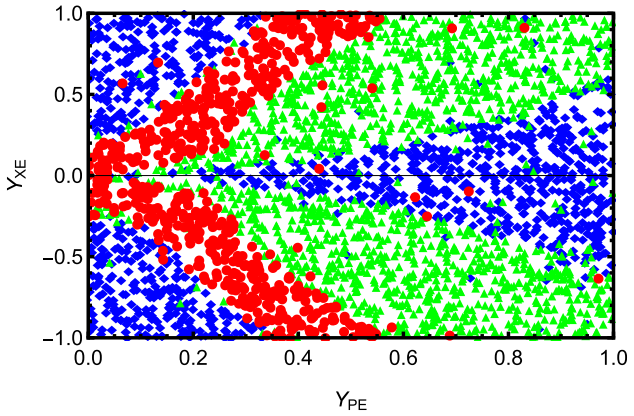

Fig. 11 $\Gamma_{NP}(h \to J/\psi Z)/\Gamma_{SM}(h \to J/\psi Z)$ in $Y_{PE} - Y_{XE}$ plane, and the marking of the scattering points represents: ♦ $(\Gamma_{NP}(h \to J/\psi Z)/\Gamma_{SM}(h \to J/\psi Z) < 1.245)$, ▲ $(1.245 \leq \Gamma_{NP}(h \to J/\psi Z)/\Gamma_{SM}(h \to J/\psi Z) < 1.255)$, ● $(1.255 \leq \Gamma_{NP}(h \to J/\psi Z)/\Gamma_{SM}(h \to J/\psi Z)$

into three regions: ♦ correspond to cases where $\Gamma_{NP}(h \to \rho Z)/\Gamma_{SM}(h \to \rho Z) < 1.26$, predominantly appearing in the low Y_{XU} region ($Y_{XU} \lesssim 0.3$) and gradually extending toward larger Y_{XD}. ▲ represent ratios in the range 1.26−1.4, with a substantially broader distribution that roughly covers the intermediate region $Y_{XU} \sim 0.2 - 0.6$. ● denote points for which the ratio exceeds 1.4, occupying almost the entire upper portion of the plane with large Y_{XU} values ($Y_{XU} \gtrsim 0.6$), and they appear densely throughout the full interval $Y_{XD} \in [0, 1]$. Overall, large values of Y_{XU} yield ratios stably above 1.4, corresponding to an enhancement exceeding 40% compared with the SM prediction.

4.4.3 The process $h \to J/\psi Z$

Thirdly, we perform a numerical analysis of the decay $h \to J/\psi Z$. The parameters are chosen as $Y_{XD} = 0.8$, $Y_{PD} = 0.01$, $Y_{XU} = 1$, $v_P = 4500$ GeV.

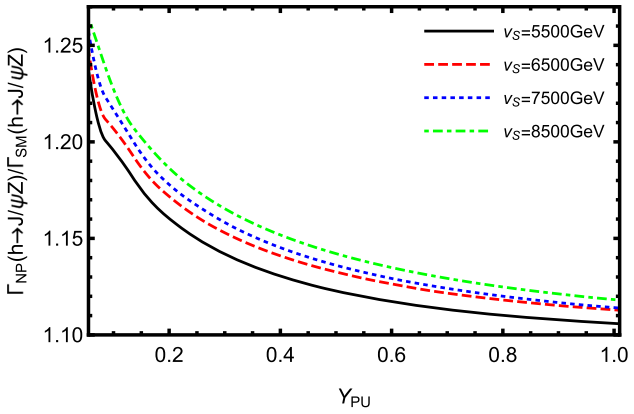

Fig. 12 $\Gamma_{NP}(h \to J/\psi Z)/\Gamma_{SM}(h \to J/\psi Z)$ varying with Y_{PU} for different v_S

We suppose the parameters with $Y_{PU} = 0.075$, $v_S = 8500$ GeV. By sampling the parameter ranges listed in Table 6, we obtain Fig. 11. In Fig. 11, the ♦, ▲ and ● correspond to $\Gamma_{NP}(h \to J/\psi Z)/\Gamma_{SM}(h \to J/\psi Z) < 1.245$, $1.245 \leq \Gamma_{NP}(h \to J/\psi Z)/\Gamma_{SM}(h \to J/\psi Z) < 1.255$ and $\Gamma_{NP}(h \to J/\psi Z)/\Gamma_{SM}(h \to J/\psi Z) \geq 1.255$, respectively. We examine the roles of Y_{PE} and Y_{XE} in Fig. 11. In the lepton sector, the parameters Y_{XE} and Y_{PE} describe the Yukawa interactions that induce couplings between SM leptons and the vector-like fermions. The points exhibit symmetry about the horizontal axis $Y_{XE} = 0$. As Y_{PE} increases from 0 to 1, $\Gamma_{NP}(h \to J/\psi Z)/\Gamma_{SM}(h \to J/\psi Z)$ first increases and then decreases. Moreover, increasing $|Y_{XE}|$ enhances the ratio symmetrically across the parameter space when $Y_{PE} > 0.2$, indicating that both positive and negative values of Y_{XE} lead to similar enhancement effects. ● show ratios consistently exceed 1.255, representing a clear deviation from the SM prediction.

For the parameter set $g_X = 0.6$, $g_{YX} = -0.1$, $Y_{XE} = 0.5$, $Y_{PE} = 0.01$, the variation of $\Gamma_{NP}(h \to J/\psi Z)/\Gamma_{SM}(h \to J/\psi Z)$ with respect to Y_{PU} is shown in Fig. 12. The black ($v_S = 5500$GeV), red ($v_S = 6500$ GeV), blue ($v_S = 7500$ GeV) and green ($v_S = 8500$ GeV) curves correspond to different choices of the singlet scalar VEV v_S. As shown in Fig. 12, all four curves exhibit a monotonically decreasing behavior as Y_{PU} increases, with the most pronounced deviations occurring in the small Y_{PU} region. In particular, for $Y_{PU} \lesssim 0.1$, the ratio $\Gamma_{NP}(h \to J/\psi Z)/\Gamma_{SM}(h \to J/\psi Z)$ reaches 1.23−1.26, corresponding to an enhancement of more than 20% over the SM prediction. As Y_{PU} continues to grow, the curves gradually flatten out. However, throughout the entire parameter range, the ratio remains above 1.10, still significantly larger than the SM value. Moreover, increasing v_S raises the overall height of the curves, indicating that a larger singlet scalar VEV further strengthens the NP contributions to the $h \to J/\psi Z$ decay.

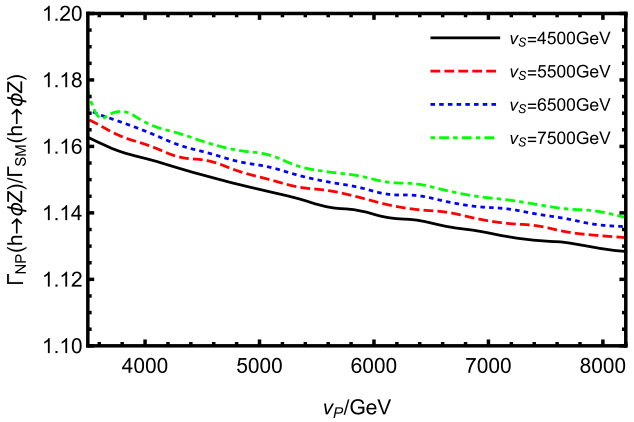

Fig. 13 $\Gamma_{NP}(h \to \phi Z)/\Gamma_{SM}(h \to \phi Z)$ varying with v_P for different v_S

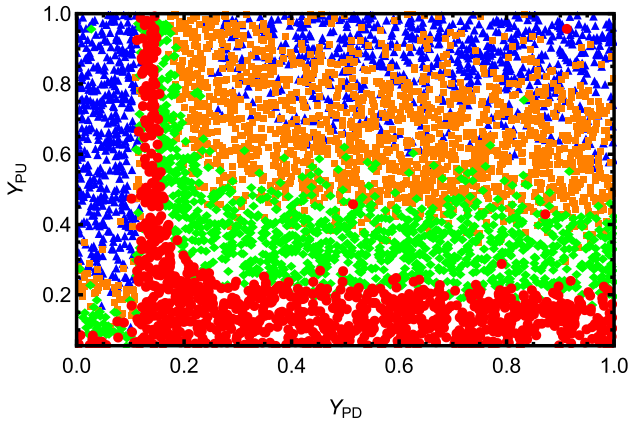

Fig. 14 $\Gamma_{NP}(h \to \phi Z)/\Gamma_{SM}(h \to \phi Z)$ in $Y_{PD} - Y_{PU}$ plane, and the marking of the scattering points represents: ▲ $(\Gamma_{NP}(h \to \phi Z)/\Gamma_{SM}(h \to \phi Z) < 1.15)$, ■ $(1.15 \leq \Gamma_{NP}(h \to \phi Z)/\Gamma_{SM}(h \to \phi Z) < 1.17)$, ♦ $(1.17 \leq \Gamma_{NP}(h \to \phi Z)/\Gamma_{SM}(h \to \phi Z) < 1.2)$, • $(1.2 \leq \Gamma_{NP}(h \to \phi Z)/\Gamma_{SM}(h \to \phi Z)$

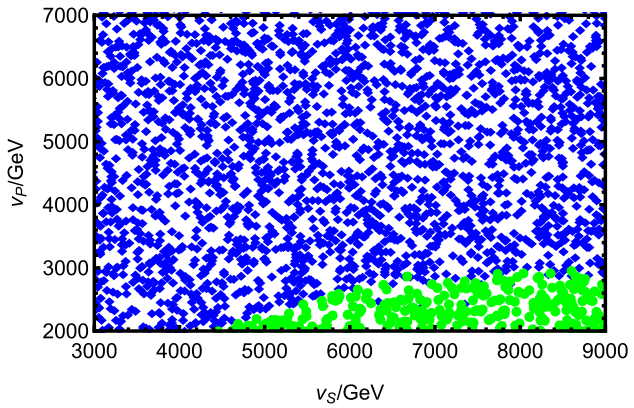

Fig. 15 $\Gamma_{NP}(h \to \Upsilon Z)/\Gamma_{SM}(h \to \Upsilon Z)$ in $v_S - v_P$ plane, and the marking of the scattering points represents: ♦ $(\Gamma_{NP}(h \to \Upsilon Z)/\Gamma_{SM}(h \to \Upsilon Z) < 1.01)$, • $(1.01 \leq \Gamma_{NP}(h \to \Upsilon Z)/\Gamma_{SM}(h \to \Upsilon Z))$

4.4.4 The process $h \to \phi Z$

Then, we analyze the decay process $h \to \phi Z$ numerically with $g_X = 0.6$, $g_{YX} = -0.1$, $Y_{XD} = 0.8$, $Y_{XU} = 1$, $Y_{XE} = 0.5$.

In Fig. 13, we fix the parameters as $Y_{PD} = 0.01$, $Y_{PU} = 0.075$, $Y_{PE} = 0.01$ and plot the ratio $\Gamma_{NP}(h \to \phi Z)/\Gamma_{SM}(h \to \phi Z)$ as a function of v_P, where v_P denotes the VEV of the singlet scalar P. From the Fig. 13, one observes that all four curves exhibit a decreasing trend. The green curve ($v_S = 7500$GeV) lies above the blue one ($v_S = 6500$ GeV), which in turn lies above the red ($v_S = 5500$ GeV), followed by the black curve ($v_S = 4500$ GeV) at the lowest position. As v_P increases, the ratio $\Gamma_{NP}(h \to \phi Z)/\Gamma_{SM}(h \to \phi Z)$ decreases, whereas increasing v_S has the opposite effect and enhances the ratio. The maximal value of the ratio reaches about 1.18, corresponding to a deviation of roughly 20% from the SM prediction.

Next, we perform a scatter analysis of the $h \to \phi Z$ process using the parameter ranges listed in Table 7. For $v_P = 4500$ GeV and $v_S = 8500$ GeV, the distribution of points in the (Y_{PD}, Y_{PU}) plane is shown in Fig. 14. The red • (corresponding to ratios larger than 1.2) are mainly concentrated in the low Y_{PU} region with $Y_{PU} \lesssim 0.25$, indicating that the NP effects are most pronounced for small Y_{PU}, where the decay width can be enhanced by more than 20% relative to the SM prediction. As Y_{PU} increases, • gradually transition into ♦ and ■, which correspond to intermediate ranges of 1.17−1.20 and 1.15−1.17, respectively. This behavior suggests that the NP contribution becomes weaker but still leads to deviations at the level of roughly 15%. Finally, in the region of larger Y_{PU}, the ▲ dominate, corresponding to ratios below 1.15, where the NP corrections are close to yet remain noticeably above the SM prediction.

Table 7 Scanning parameters for Fig. 14

Parameters	Min	Max
Y_{PD}	0	1
Y_{PU}	0.055	1
Y_{PE}	0	1

4.4.5 The process $h \to \Upsilon Z$

At last, we carry out a numerical analysis of the decay $h \to \Upsilon Z$. As a heavy vector meson, Υ is composed of a $b\bar{b}$ pair.

With the parameter choices $g_X = 0.6$, $g_{YX} = -0.1$, $Y_{XD} = 0.8$, $Y_{PD} = 0.01$, $Y_{XU} = 1$, $Y_{PU} = 0.075$, $Y_{XE} = 0.5$, $Y_{PE} = 0.01$, we investigate the impact of v_S and v_P on the ratio $\Gamma_{\rm NP}(h \to \Upsilon Z)/\Gamma_{\rm SM}(h \to \Upsilon Z)$. The results are shown in Fig. 15, based on the scan ranges

Table 8 Scanning parameters for Fig. 15

Parameters	Min	Max
v_S/GeV	3000	9000
v_P/GeV	2000	7000

provided in Table 8. The ♦ and • denote regions with $\Gamma_{NP}(h \to \Upsilon Z)/\Gamma_{SM}(h \to \Upsilon Z) < 1.01$ and $1.01 \leq \Gamma_{NP}(h \to \Upsilon Z)/\Gamma_{SM}(h \to \Upsilon Z)$, respectively. It can be observed that the larger corrections (•) occur predominantly in the lower right region of the parameter plane. This indicates that larger values of v_S combined with smaller values of v_P enhance the NP contributions. The ratio reaches values in the range of approximately 1.01−1.35. For the decay $h \to \Upsilon Z$, the magnitude of the NP effects is smaller than in the other processes considered.

5 Discussion and conclusion

In summary, the $U(1)_X$VLFM model introduces an additional Abelian gauge symmetry and one generation of vectorlike fermions, leading to a noticeable modification of the Higgs gauge interaction structure compared with the SM. The right-handed neutrinos and the two singlet Higgs fields included in the model can realize the seesaw mechanism within a non-supersymmetric framework, while the extended fermion spectrum also provides new contributions to Higgs related loop effects. Within this framework, we perform a detailed analysis of the rare decay $h \to Z\gamma$ as well as the hadronic channels $h \to m_V Z$ with $m_V = \rho, \omega, \phi, J/\psi, \Upsilon$. For completeness, numerical results for $h \to \gamma\gamma$ and $h \to VV^*(V = Z, W)$ are also evaluated to assess the broader impact of NP on Higgs decay patterns. In the SM, the hZZ coupling appears at tree level, whereas the $h\gamma Z$ coupling arises only through loop contributions. For the decay $h \to m_V Z$, the amplitude receives both direct and indirect contributions. The direct contribution corresponds to the Higgs coupling to quarks that hadronize directly into the final state vector meson, while the indirect contribution originates from the Higgs coupling to an on-shell Z boson and an off-shell gauge boson (γ or Z), which subsequently converts into the vector meson. As pointed out in Ref. [22], the indirect contribution is typically much larger than the direct one in the viable parameter space. Beyond the SM, the $h\gamma Z$ vertex can receive new CP-even and CP-odd effective couplings $C_{\gamma Z}$ and $\tilde{C}_{\gamma Z}$, although the CP-even part usually remains dominant. In this work, we compute their contributions to the $h\gamma Z$ vertex using the effective Lagrangian approach.

In the SM, the Higgs boson couples to the W and Z gauge bosons at tree level, while its interaction with photons arises only through loop diagrams. Consequently, the decay channels $h \to \gamma\gamma$, $h \to WW^*$ and $h \to ZZ^*$ exhibit high sensitivity in experimental measurements, with the observed signal strengths $R_{\gamma\gamma} = 1.10 \pm 0.06$, $R_{WW^*} = 1.00 \pm 0.08$, $R_{ZZ^*} = 1.02 \pm 0.08$ [58–62]. The dominant contributions to the processes $h \to ZZ^*$, $h \to \gamma\gamma$ and $h \to Z\gamma$ all originate from similar one loop topologies. Within the $U(1)_X$VLFM framework examined in this work, the NP corrections to $h \to \gamma\gamma$ typically fall in the range 1.0−1.2, while those for $h \to VV^*(V = Z, W)$ are around 1.1. Unlike $h \to \gamma\gamma$ and $h \to Z\gamma$, which are purely loop induced and sensitive only to charged particles running in the loop, the decay $h \to ZZ^*$ also receives a tree level contribution from the hZZ vertex and allows neutral particles to participate in the loop diagrams. Despite these differences, the three decay channels remain structurally very similar. It is worth emphasizing that the combined ATLAS and CMS analysis reports a signal strength of $\mu_{Z\gamma} = 2.2 \pm 0.7$ for $h \to Z\gamma$, significantly higher than the SM expectation and reaching the level of experimental evidence [18]. This deviation further motivates the study of possible NP effects in $h \to Z\gamma$ and in the related $h \to m_V Z$ decay channels.

The numerical analysis shows that the NP correction to $h \to Z\gamma$ can reach up to 65% compared with the SM prediction. For the decays $h \to \omega Z$ and $h \to \rho Z$, the NP contributions lie in the range of 20–70%, while for $h \to \phi Z$ and $h \to J/\psi Z$, the corrections are typically 10%-25%. Among the vector mesons considered in this study (ρ, ω, ϕ, J/ψ, Υ), the Υ is the heaviest. Although we tried adjusting many parameters in an attempt to enhance the deviation in $h \to \Upsilon Z$, the NP contribution to this process remains rather small. Overall, our results suggest a clear trend: NP effects in $h \to m_V Z$ are more pronounced when the final state vector meson is light. Considering that $\Gamma_{NP}(h \to Z\gamma)/\Gamma_{SM}(h \to Z\gamma) \approx 1.65$, the fact that the NP corrections to the rare decays $h \to m_V Z$ can improve about 70% of the SM prediction represents a sizable deviation.

In NP scenarios, the additional interactions can modify the SM CP-even coupling and may also introduce CP-odd contributions, thereby enhancing the branching ratio of the rare decay $h \to m_V Z$. Since this decay is intrinsically rare, the current experimental sensitivity is still insufficient for detection. However, its branching ratio can be reliably calculated at the theoretical level, and it may become observable at the HL-LHC and future high-energy colliders. Therefore, the decay channels $h \to m_V Z$ provide an important opportunity to test the $U(1)_X$VLFM model and to explore possible NP effects in the Higgs sector.

Acknowledgements This work is supported by National Natural Science Foundation of China (NNSFC) (No.12075074), Natural Science Foundation of Hebei Province (A2023201040, A2022201022,

A2022201017, A2023201041), Natural Science Foundation of Hebei Education Department (QN2022173), the Project of the China Scholarship Council (CSC) No. 202408130113. This work is also supported by Fundação para a Ciência e a Tecnologia (FCT, Portugal) through the project UID/00777/2025 (https://doi.org/10.54499/UID/00777/2025).

Data Availability Statement Data will be made available on reasonable request. [Authors' comment: The datasets generated during and/or analysed during the current study are available from the corresponding author on reasonable request.]

Code Availability Statement Code/software will be made available on reasonable request. [Authors' comment: The code/software generated during and/or analysed during the current study is available from the corresponding author on reasonable request.]

Funded by SCOAP[3].

Appendix A: Mass matrix and coupling in $U(1)_X$VLFM

The mass matrix for up-type quark in the (u_L, u_{XL}), (u_R^*, u_{XR}^*) basis reads

$$m_u = \begin{pmatrix} \frac{1}{\sqrt{2}} v Y_u^T & 0 \\ \frac{1}{\sqrt{2}} v_S Y_{XU}^T & \frac{1}{\sqrt{2}} v_P Y_{PU}^T \end{pmatrix}. \tag{A1}$$

We diagonalize the mass matrix using U_L^u and U_R^u

$$U_L^{u,*}\, m_u\, U_R^{u,\dagger} = m_u^{dia}. \tag{A2}$$

In the (e_L, e_{XL}), (e_R^*, e_{XR}^*) basis, the lepton mass matrix is given by

$$m_e = \begin{pmatrix} \frac{1}{\sqrt{2}} v Y_e^T & 0 \\ \frac{1}{\sqrt{2}} v_S Y_{XE}^T & \frac{1}{\sqrt{2}} v_P Y_{PE}^T \end{pmatrix}. \tag{A3}$$

This matrix is diagonalized by U_L^e and U_R^e

$$U_L^{e,*}\, m_e\, U_R^{e,\dagger} = m_e^{dia}. \tag{A4}$$

Other Higgs-related vertices are included as follows

$$\begin{aligned}
\mathcal{L}_{h_k \bar{e}_i e_j} = \bar{e}_i \Big\{ & -i \frac{1}{\sqrt{2}} \Big(\sum_{b=1}^{3} \sum_{a=1}^{3} U_{L,jb}^{e,*} U_{R,ia}^{e,*} Y_{e,ab} Z_{k1}^H \\
& + U_{L,j4}^{e,*} \sum_{a=1}^{3} U_{R,ia}^{e,*} Y_{XE,a1} Z_{k2}^H + U_{L,j4}^{e,*} U_{R,i4}^{e,*} Y_{PE} Z_{k3}^H \Big) P_L \\
& - i \frac{1}{\sqrt{2}} \Big(\sum_{b=1}^{3} \sum_{a=1}^{3} U_{R,ja}^{e} U_{L,ib}^{e} Y_{e,ab}^* Z_{k1}^H + U_{L,i4}^{e} \sum_{a=1}^{3} \\
& U_{R,ja}^{e} Y_{XE,a1}^* Z_{k2}^H + U_{R,j4}^{e} U_{L,i4}^{e} Y_{PE}^* Z_{k3}^H \Big) P_R \Big\} e_j h_k,
\end{aligned} \tag{A5}$$

$$\begin{aligned}
\mathcal{L}_{h_k \bar{d}_i d_j} = \bar{d}_i \Big\{ & -i \frac{1}{\sqrt{2}} \Big(\sum_{b=1}^{3} \sum_{a=1}^{3} U_{L,jb}^{d,*} U_{R,ia}^{d,*} Y_{d,ab} Z_{k1}^H \\
& + U_{L,j4}^{d,*} \sum_{a=1}^{3} U_{R,ia}^{d,*} Y_{XD,a1} Z_{k2}^H + U_{L,j4}^{d,*} U_{R,i4}^{d,*} Y_{PD} Z_{k3}^H \Big) P_L \\
& - i \frac{1}{\sqrt{2}} \Big(\sum_{b=1}^{3} \sum_{a=1}^{3} U_{R,ja}^{d} U_{L,ib}^{d} Y_{d,ab}^* Z_{k1}^H + U_{L,i4}^{d} \\
& \sum_{a=1}^{3} U_{R,ja}^{d} Y_{XD,a1}^* Z_{k2}^H + U_{R,j4}^{d} U_{L,i4}^{d} Y_{PD}^* Z_{k3}^H \Big) P_R \Big\} d_j h_k,
\end{aligned} \tag{A6}$$

$$\begin{aligned}
\mathcal{L}_{h_k \bar{u}_i u_j} = \bar{u}_i \Big\{ & -i \frac{1}{\sqrt{2}} \Big(\sum_{b=1}^{3} \sum_{a=1}^{3} U_{L,jb}^{u,*} U_{R,ia}^{u,*} Y_{u,ab} Z_{k1}^H + U_{L,j4}^{u,*} \\
& \sum_{a=1}^{3} U_{R,ia}^{u,*} Y_{XU,a1} Z_{k2}^H + U_{L,j4}^{u,*} U_{R,i4}^{u,*} Y_{PU} Z_{k3}^H \Big) P_L \\
& - i \frac{1}{\sqrt{2}} \Big(\sum_{b=1}^{3} \sum_{a=1}^{3} U_{R,ja}^{u} U_{L,ib}^{u} Y_{u,ab}^* Z_{k1}^H + U_{L,i4}^{u} \sum_{a=1}^{3} \\
& U_{R,ja}^{u} Y_{XU,a1}^* Z_{k2}^H + U_{R,j4}^{u} U_{L,i4}^{u} Y_{PU}^* Z_{k3}^H \Big) P_R \Big\} u_j h_k,
\end{aligned} \tag{A7}$$

with

$$Y_{XE,a1} = \begin{pmatrix} 0 \\ 0 \\ Y_{XE} \end{pmatrix}, \quad Y_{XD,a1} = \begin{pmatrix} 0 \\ 0 \\ Y_{XD} \end{pmatrix}, \quad Y_{XU,a1} = \begin{pmatrix} 0 \\ 0 \\ Y_{XU} \end{pmatrix}. \tag{A8}$$

Appendix B: Anomaly cancellation in $U(1)_X$VLFM

Since all SM fields carry zero $U(1)_X$ charge, they do not contribute to anomalies involving $U(1)_X$. Therefore, the anomaly cancellation relies entirely on the newly introduced fermions, whose gauge quantum numbers are listed in Table 1. Below we show explicitly that all relevant anomalies cancel.

1. $[U(1)_X]^3$ anomaly

The cubic $U(1)_X$ anomaly is given by the sum of the cube of the $U(1)_X$ charges of all chiral fermions. Since the SM fields are neutral under $U(1)_X$, only the new fermions contribute:

$$\begin{aligned}\sum_n (Y_n^X)^3 &= \underbrace{(Q_a)^3\times 3}_{d_{XL}} + \underbrace{(-Q_a)^3\times 3}_{u_{XL}} + \underbrace{(Q_b)^3\times 3}_{d_{XR}} + \underbrace{(-Q_b)^3\times 3}_{u_{XR}} \\ &\quad + \underbrace{(Q_a)^3}_{e_{XL}} + \underbrace{(-Q_a)^3}_{\nu_{XL}} + \underbrace{(Q_b)^3}_{e_{XR}} + \underbrace{(-Q_b)^3}_{\nu_{XR}} \\ &= 3(Q_a^3 - Q_a^3) + 3(Q_b^3 - Q_b^3) \\ &\quad + (Q_a^3 - Q_a^3) + (Q_b^3 - Q_b^3) = 0. \end{aligned} \tag{B1}$$

Here the factor 3 arises from the color multiplicity of the quarks. The cancellation occurs automatically and is independent of the specific values of Q_a and Q_b.

2. Gravitational$-U(1)_X$ anomaly

The mixed gravitational anomaly is proportional to the sum of the $U(1)_X$ charges of all chiral fermions:

$$\sum_n Y_n^X = \underbrace{Q_a\times 3}_{d_{XL}} + \underbrace{(-Q_a)\times 3}_{u_{XL}} + \underbrace{Q_b\times 3}_{d_{XR}} + \underbrace{(-Q_b)\times 3}_{u_{XR}} \tag{B2}$$

$$+ \underbrace{Q_a}_{e_{XL}} + \underbrace{(-Q_a)}_{\nu_{XL}} + \underbrace{Q_b}_{e_{XR}} + \underbrace{(-Q_b)}_{\nu_{XR}} = 0. \tag{B3}$$

3. $[SU(3)_C]^2U(1)_X$ anomaly

Only colored fermions contribute to this anomaly. Since SM quarks have $U(1)_X$=0, only the new vector-like quarks contribute:

$$\sum_q Y_q^X = \underbrace{Q_a\times 3}_{d_{XL}} + \underbrace{(-Q_a)\times 3}_{u_{XL}} + \underbrace{Q_b\times 3}_{d_{XR}} + \underbrace{(-Q_b)\times 3}_{u_{XR}} = 0. \tag{B4}$$

4. $[SU(2)_L]^2U(1)_X$ anomaly

This anomaly receives contributions only from $SU(2)_L$ doublets. Since all newly introduced fermions are $SU(2)_L$ singlets and the SM doublets carry zero $U(1)_X$ charge, the anomaly vanishes trivially:

$$\sum_L Y_L^X = 0. \tag{B5}$$

5. Mixed Abelian anomalies

(a) $U(1)_Y[U(1)_X]^2$

$$\begin{aligned}\sum_n Y_n^Y (Y_n^X)^2 &= \underbrace{\left(-\frac{1}{3}\right)(Q_a)^2\times 3}_{d_{XL}} + \underbrace{\left(\frac{2}{3}\right)(-Q_a)^2\times 3}_{u_{XL}} \\ &\quad + \underbrace{\left(\frac{1}{3}\right)(Q_b)^2\times 3}_{d_{XR}} + \underbrace{\left(-\frac{2}{3}\right)(-Q_b)^2\times 3}_{u_{XR}} \\ &\quad + \underbrace{(-1)(Q_a)^2}_{e_{XL}} + \underbrace{0}_{\nu_{XL}} + \underbrace{(1)(Q_b)^2}_{e_{XR}} + \underbrace{0}_{\nu_{XR}} \\ &= 3\left(-\frac{1}{3}Q_a^2 + \frac{2}{3}Q_a^2 + \frac{1}{3}Q_b^2 - \frac{2}{3}Q_b^2\right) + (-Q_a^2 + Q_b^2) \\ &= (Q_a^2 - Q_b^2) + (-Q_a^2 + Q_b^2) = 0. \end{aligned} \tag{B6}$$

(b) $[U(1)_Y]^2U(1)_X$

$$\begin{aligned}\sum_n (Y_n^Y)^2 Y_n^X &= \underbrace{\left(-\frac{1}{3}\right)^2 Q_a\times 3}_{d_{XL}} + \underbrace{\left(\frac{2}{3}\right)^2(-Q_a)\times 3}_{u_{XL}} \\ &\quad + \underbrace{\left(\frac{1}{3}\right)^2 Q_b\times 3}_{d_{XR}} + \underbrace{\left(-\frac{2}{3}\right)^2(-Q_b)\times 3}_{u_{XR}} \\ &\quad + \underbrace{(-1)^2 Q_a}_{e_{XL}} + \underbrace{0}_{\nu_{XL}} + \underbrace{(1)^2 Q_b}_{e_{XR}} + \underbrace{0}_{\nu_{XR}} \\ &= 3\left(\frac{1}{9}Q_a - \frac{4}{9}Q_a + \frac{1}{9}Q_b - \frac{4}{9}Q_b\right) + (Q_a + Q_b) \\ &= (-Q_a - Q_b) + (Q_a + Q_b) = 0. \end{aligned} \tag{B7}$$

From the above calculations, all gauge anomalies involving $U(1)_X$, including $[U(1)_X]^3$, gravitational$-U(1)_X$, $[SU(3)_C]^2U(1)_X$, $[SU(2)_L]^2U(1)_X$, and the mixed Abelian anomalies $U(1)_Y[U(1)_X]^2$ and $[U(1)_Y]^2U(1)_X$ cancel exac tly. Therefore, the $U(1)_X$VLFM model is anomaly free.

References

1. G. Aad et al. [ATLAS], Phys. Lett. B **716**, 1–29 (2012)
2. S. Chatrchyan et al. [CMS], Phys. Lett. B **716**, 30–61 (2012)
3. K. Abe et al. [T2K], Phys. Rev. Lett. **107**, 041801 (2011)
4. F.P. An et al. [Daya Bay], Phys. Rev. Lett. **108**, 171803 (2012)
5. S. Navas et al. [Particle Data Group], Phys. Rev. D **110**, 030001 (2024)
6. H.E. Haber, G.L. Kane, Phys. Rep. **117**, 75 (1985)
7. G.C. Branco, P.M. Ferreira, L. Lavoura et al., Phys. Rep. **516**, 1–102 (2012)
8. S.P. Martin, Adv. Ser. Direct. High Energy Phys. **18**, 1–98 (1998)
9. M. Maniatis, Int. J. Mod. Phys. A **25**, 3505–3602 (2010)
10. G. Panico, A. Wulzer, Lect. Notes Phys. **913**, 1–316 (2016)
11. J. Rosiek, Phys. Rev. D **41**, 3464 (1990)
12. H.P. Nilles, Phys. Rep. **110**, 1 (1984)
13. D.N. Gao, Phys. Lett. B **737**, 366 (2014)
14. T. Modak, R. Srivastava, Mod. Phys. Lett. A **32**, 1750004 (2017)
15. A. Djouadi, J. Kalinowski, M. Spira, Comput. Phys. Commun. **108**, 56 (1998)
16. D. de Florian et al., CERN Yellow Rep. Monogr. **2**, 1–869 (2017)
17. G. Degrassi, M. Vitti, Eur. Phys. J. C **80**(4), 307 (2020)
18. G. Aad et al. [ATLAS and CMS], Phys. Rev. Lett. **132**, 021803 (2024)
19. A.L. Kagan, G. Perez, F. Petriello et al., Phys. Rev. Lett. **114**, 101802 (2015)
20. G.T. Bodwin, H.S. Chung, J.H. Ee et al., Phys. Rev. D **90**, 113010 (2014)
21. M. Konig, M. Neubert, JHEP **08**, 012 (2015)
22. S. Alte, M. Koniga, M. Neubert, JHEP **12**, 037 (2016)
23. G. Isidori, A.V. Manohar, M. Trott, Phys. Lett. B **728**, 131 (2014)
24. M.G. Alonso, G. Isidori, Phys. Lett. B **733**, 359 (2014)
25. G.P. Lepage, S.J. Brodsky, Phys. Lett. B **87**, 359 (1979)
26. G.P. Lepage, S.J. Brodsky, Phys. Rev. D **22**, 2157 (1980)
27. A.V. Efremov, A.V. Radyushkin, Phys. Lett. B **94**, 245 (1980)
28. V.L. Chernyak, A.R. Zhitnitsky, Phys. Rep. **112**, 173 (1984)
29. A.M. Sirunyan et al. [CMS], **11**, 039 (2020)
30. A. Tumasyan et al. [CMS], Phys. Lett. B **842**, 137534 (2023)

31. G. Bélanger, C. Delaunay, S. Westhoff, Phys. Rev. D **92**, 055021 (2015)
32. G. Bélanger, C. Delaunay, Phys. Rev. D **94**(7), 075019 (2016)
33. S.Q. Dinh, H.M. Tran, Phys. Rev. D **104**(11), 115009 (2021)
34. T.M. Hieu, Q.S. Sang, T.Q. Trang, Commun. Phys. **30**(3), 231–244 (2020)
35. S.Q. Dinh, H.M. Tran, Nucl. Phys. B **997**, 116384 (2023)
36. J.A. Aguilar-Saavedra, R. Benbrik, S. Heinemeyer et al., Phys. Rev. D **88**(9), 094010 (2013)
37. J. Cao, L. Meng, L. Shang et al., Phys. Rev. D **106**(5), 055042 (2022)
38. Q.H. Cao, J. Guo, J. Liu et al., Phys. Rev. D **110**(1), 015029 (2024)
39. M. Lindner, D. Schmidt, A. Watanabe, Phys. Rev. D **89**(1), 013007 (2014)
40. S. Iwamoto, T.J. Kärkkäinen, Z. Péli et al., Phys. Rev. D **104**(5), 055042 (2021)
41. S.P. Chen, P.H. Gu, Nucl. Phys. B **986**, 116057 (2023)
42. S. Centelles Chuliá, A. Herrero-Brocal, A. Vicente, JHEP **07**, 060 (2024)
43. M.E. Peskin, D.V. Schroeder, *An Introduction to Quantum Field Theory* (Addison Wesley, Reading, 1995)
44. P.H. Chankowski, S. Pokorski, J. Wagner, Eur. Phys. J. C **47**, 187–205 (2006)
45. G. Bélanger, J. Da Silva, H.M. Tran, Phys. Rev. D **95**(11), 115017 (2017)
46. B. Bhattacharya, A. Datta, D. London, Phys. Lett. B **736**, 421–427 (2014)
47. L. Bergstrom, G. Hulth, Nucl. Phys. B **259**, 137 (1985). [Erratum ibid. B 276 (1986) 744]
48. M. Spira, A. Djouadi, P.M. Zerwas, Phys. Lett. B **276**, 350 (1992)
49. V.L. Chernyak, A.R. Zhitnitsky, Nucl. Phys. B **201**, 2182 (1996)
50. N.H. Fuchs, M.D. Scadron, Phys. Rev. D **20**, 2421 (1979)
51. M. Beneke, G. Buchalla, M. Neubert, C.T. Sachrajda, Nucl. Phys. B **591**, 313 (2000)
52. R. Benbrik, M. Boukidi, M. Ech-chaouy et al., JHEP **03**, 020 (2025)
53. V. Chekhovsky et al. [CMS], JHEP **08**, 156 (2025)
54. G. Aad et al. [ATLAS], Eur. Phys. J. C **85**(11), 1335 (2025)
55. G. Aad et al. [ATLAS], Phys. Lett. B **796**, 68–87 (2019)
56. G. Cacciapaglia, C. Csaki, G. Marandella et al., Phys. Rev. D **74**, 033011 (2006)
57. M. Carena, A. Daleo, B.A. Dobrescu et al., Phys. Rev. D **70**, 093009 (2004)
58. G. Aad et al. [ATLAS and CMS], JHEP **08**, 045 (2016)
59. G. Aad et al. [ATLAS], JHEP **07**, 088 (2023)
60. A. Tumasyanet et al. [CMS], Nature **607**(7917), 60–68 (2022)
61. T. Aaltonen et al. [CDF and D0], Phys. Rev. D **88**(5), 052014 (2013)
62. G. Aad et al. [ATLAS], Eur. Phys. J. C **80**(10), 957 (2020)